International Journal of Impact Engineering 191 (2024) 104991

Contents lists available at ScienceDirect

International Journal of Impact Engineering

journal homepage: www.elsevier.com/locate/ijimpeng

Effect of the loading-rate and stress state on the constitutive modelling and fracture of 2205 Duplex stainless steel

D. Abedul [a,*], L. Galdos [a], E. Sáenz de Argandoña [a], F. Galvez [b], B. Erice [a,c]

[a] Mondragon Unibertsitatea, Faculty of Engineering, Department of Mechanics and Industrial Production, Loramendi 4, Arrasate-Mondragon 20500, Gipuzkoa, Spain
[b] Department of Materials Science, E.T.S.I. de Caminos, Canales y Puertos, Universidad Politécnica de Madrid (UPM), Profesor Aranguren 3, 28040 Madrid, Spain
[c] IKERBASQUE, Basque Foundation for Science, Bilbao, Spain

ARTICLE INFO

Keywords:
2205 Duplex Stainless steel
Ductile fracture
Stress state
Strain rate
Temperature

ABSTRACT

Shear cutting is a high-speed forming process where material separation is involved. The nature of the process leads to high strain rates and temperatures on the sheared zone of the material subjected to the operation. In this work, the mechanical behavior in terms of flow stress, plastic deformation and fracture of a 2205 Duplex stainless steel sheet is determined. Uniaxial tension, uniaxial compression, stack compression, plane strain tension and simple shear tests at different angles with respect to the rolling direction of the metal sheet are performed to determine the anisotropic behavior of the material. Strain rate and temperature dependence of the flow stress and the plastic behavior of the material is determined through notched tensile tests performed under various temperatures (20°C, 100°C, 300°C and 500°C) and strain rates (0.001 s^{-1}, 10 s^{-1} and >100 s^{-1}). Finally, fracture behavior under various stress states is determined through notched tensile, central hole, in-plane shear and plane strain tests. The temperature and strain rate dependence of the fracture behavior is determined through notched tensile, in-plane shear and plane strain tests performed under various temperatures (20°C, 100°C, 300°C and 500°C) and strain rates (0.001 s^{-1}, 10 s^{-1} and >100 s^{-1}). The anisotropic behavior and work hardening of the material are modelled by the Hill48 yield function and Swift-Hockett-Sherby hardening law, respectively. Among the two ductile fracture models tested, Hosford-Coulomb model showed the best agreement and is therefore used to account for the temperature and strain rate effects on the fracture behavior. By combining these three models, an accurate reproduction of the mechanical behavior of the 2205 Duplex stainless steel sheet is achieved.

1. Introduction

Shear cutting processes are commonly employed in the manufacturing industry to eliminate scraps or to convert a metal coil into various sheets with precise dimensions. In this mechanical process, a part is separated into two or more pieces by using a pair of knives or a punch and die set to deform the material until it fractures. Since a large portion of the plastic work is converted into heat during cutting, the material's temperature increases [1]. Additionally, shear cutting processes are performed at high speeds to meet production requirements, resulting in large strains, high strain rates and high temperatures during these metal forming operations. To accurately analyze these processes, it is essential to characterize the material subjected to the cutting operations, taking into account temperature and strain rate effects to capture all the occurring phenomena [2,3]. This research aims to provide a detailed characterization of a 5 mm thick 2205 Duplex stainless steel sheet, analyzing its anisotropy, work hardening and fracture behavior and proposing a material model for Finite Element (FE) simulations.

Anisotropic yield criteria are essential in the simulation and analysis of metal forming processes, particularly in those that involve metal sheets. The production of metal sheets typically involves one or more rolling stages, which can be performed at either cold or hot temperatures, resulting in different mechanical properties in different directions [4]. Over the years, various models have been proposed and utilized to represent this type of mechanical behavior in numerical simulations of metal forming processes. Hill48 yield criterion [5], which is the most well-known anisotropic yield function, has been applied in numerous metal forming studies, such as press bending and roll forming [6], warm forming [7] or open cutting line shear cutting [8]. However, further research on the anisotropic behavior of metals has revealed the limitations of Hill48's flexibility, leading to the development of more flexible alternatives that can fit more complex yield surfaces. Examples of such

* Corresponding author.
E-mail address: dabedul@mondragon.edu (D. Abedul).

https://doi.org/10.1016/j.ijimpeng.2024.104991
Received 24 November 2023; Received in revised form 14 February 2024; Accepted 1 May 2024
Available online 3 May 2024

models include Yld2000 model [9], which aims to represent the behavior of aluminum alloys, BBC2005 model [10] and Yoshida-Uemori model [11]. These models are widely used in both industrial and research settings [12–16], and some are even included as default options in commercial FE codes.

In addition to accurately determining the transition between elastic and plastic behavior, the work hardening of the material is also essential to analyze metal forming processes as most of them involve plastic deformation of the material subjected to the forming operation. There are different types of work hardening models to represent this behavior, such as isotropic models, kinematic models and combined models. Isotropic models assume that the material hardens equally in all directions (expansion of the yield surface), kinematic models consider the effects of the previous loading history of the material (translation of the yield surface) and combined models allow both the expansion and translation of the yield surface in the stress domain [17]. In this study isotropic hardening models are considered as the studied material is not subjected to previous deformation. There are a wide range of proposed equations that can be used to represent the expansion of the yield surface. From the most simple proposals like Hollomon hardening law [18] and its evolutions Ludwik [19] and Swift [20] models, to more complex hardening laws like Swift-Voce [21], Hensel-Spittel [22] or Swift-Hockett-Sherby [14]. Larger degrees of complexity can be added to the equations by including the temperature or strain rate effects. For instance, the model proposed by Johnson and Cook consists in adding these effects to Ludwik's model [23]. Indeed, the temperature and strain rate sensitivity terms introduced in this model have been widely included in other hardening laws to represent the effect of both parameters [12,21,24,25].

Lastly, the behavior of the material towards fracture is another important factor to take into account as shear cutting processes involve material separation. Since the studied material is a stainless steel, which can be considered as a ductile metal, fracture criteria for brittle materials are not applicable in this work. Ductile fracture is considered to be highly influenced by the stress state of the material, often expressed through the stress triaxiality η [26–28] and more recently combining it with the third deviatoric stress invariant through the normalized third deviatoric stress invariant ξ or the Lode angle parameter $\overline{\theta}$ [29–31]. This approach to model ductile fracture has led to a great number of models which compute the fracture plastic strain $\overline{\varepsilon}_p^f$ as a function of these stress parameters. For instance, the ductile fracture model recently proposed by Lou et al., DF2016 [32] or Hosford-Coulomb model [33], which is widely used by the scientific community to model ductile fracture behavior due to its flexibility to adapt the fracture surface in the triaxiality domain [12,21,24,25,34]. Furthermore, some researchers went one step further by including the effect of strain rate [12,21,34–37] or the effect of temperature [3,38] on the modelling of the fracture behavior of the material being studied. Some authors even considered the effect of both phenomena simultaneously on either steels or aluminum alloys [24,25,39–41]. To achieve this, the authors modified the ductile fracture model considered in their works by incorporating terms to account for the material's behavior under high strain rates and/or high temperatures during its service.

The importance of considering temperature and strain rate effects in FE simulations of shear cutting processes remains a debated topic. To address this issue, this study presents a thermomechanical characterization of a 5 mm thick 2205 Duplex stainless steel sheet. The characterization includes the analysis of the anisotropic behavior of the material in quasi-static and room temperature conditions at various stress states, its work hardening behavior at different temperatures (20°C – 500°C) and strain rates (0.001 s^{-1} – >100 s^{-1}) in the rolling direction and its fracture behavior at different stress states, temperatures (20°C – 500°C) and strain rates (0.001 s^{-1} – >100 s^{-1}). The results obtained are used to calibrate models capable of accurately represent the material's behavior in FE simulations. Anisotropic behavior is modelled through Hill48 anisotropic yield criterion. Swift-Hockett-Sherby work hardening model is calibrated in quasi-static and room temperature conditions and modified to include the effects of temperature and strain rate by means of the terms proposed by Johnson and Cook [23]. To model the material's fracture behavior, two proportional ductile fracture models (DF2016 and Hosford-Coulomb) are used considering the non-proportionality of the loading path to fracture observed in the characterization tests. Finally, the model that better fits the experimental data is modified to account for the temperature and strain rate effect on the predicted fracture loci.

2. Experimental methodology

2.1. Material and specimens

This research focuses on the behavior of a 5 mm thick 2205 Duplex stainless steel sheet. The sheet underwent several forming processes and heat treatments during its manufacture, including hot rolling, annealing, pickling and roll levelling. All specimens tested in this work are sourced from the same material coil provided by Acerinox S.A. The microstructure of 2205 Duplex stainless steel consists of roughly an equal mix of ferrite (grey) and austenite (white) phases (see Fig. 1). The chemical composition of the supplied material is shown in Table 1.

The anisotropic behavior of the material is assessed under quasi-static and room temperature conditions across various stress states and directions. The work hardening and fracture behavior of the material is evaluated at different stress states, temperatures (20°C, 100°C, 300°C and 500°C) and strain rates (0.001 s^{-1}, 10 s^{-1} and >100 s^{-1}). To ensure the repeatability of the results, at least three experiments are performed for each test configuration, and average values are computed. All the specimens are manufactured through Wire Electrical Discharge Machining (WEDM). The specimens utilized to study the material anisotropy are machined at different orientations with respect to the rolling direction (RD), while the rest are extracted only in the RD. The following specimens are tested: UT – Uniaxial Tension [42], SC – Stack compression [9], UC – Uniaxial Compression [43], CH – Central Hole [44], SH – Shear (2 geometries) [37,38,45], PS – Plane Strain (2 geometries) [31] and NT – Notched Tensile (3 geometries) [7,21]. The geometry and dimension of these specimens are depicted in Fig. 2.

2.2. Experimental setups

The quasi-static and room temperature tests are conducted in a MTS 810 Universal Testing Machine (UTM) equipped with a 100 kN load cell

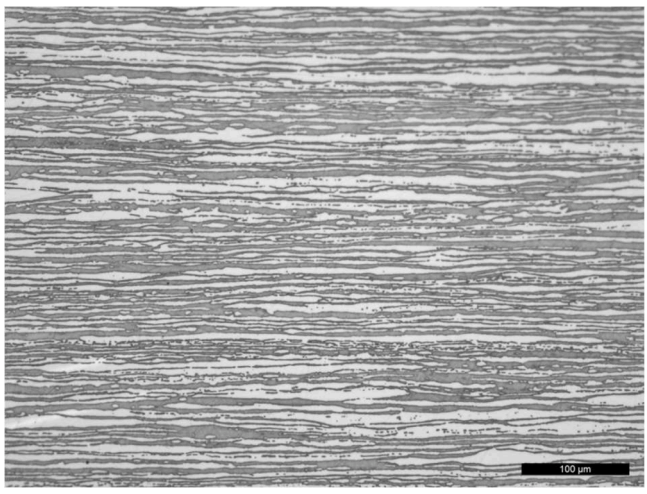

Fig. 1. As-received microstructure of the 2205 Duplex stainless steel sheet with ferrite phase in grey color and austenite phase in white color.

Table 1
Chemical composition of 2205 Duplex stainless steel (wt.%).

C	Si	Mn	P	S	Cr	Ni	Mo	N
≤0.03	≤1	≤2	≤0.035	≤0.015	22 – 23	4.5 – 6.5	3 – 3.5	0.14 – 0.2

under displacement control. The crosshead velocities used in the quasi-static tests are determined by computing the nominal strain rate. For the quasi-static experiments, the crosshead velocities were calculated such that the nominal strain rate over the specimen gage length in the case of the tensile tests, and over the height in the case of the compression tests, gave 0.001 s^{-1}. In the intermediate tests, the maximum crosshead velocity achievable by the servo-hydraulic machine (MTS) was employed. However, the These velocities and frame and data acquisition rates used for each specimen geometry are summarized in Table 2. Except in the case of the SC and UC tests, a black and white speckle pattern is applied to the surface of the specimens to measure the displacement fields with Digital Image Correlation (DIC) on images captured by a JAI GO-5000M-USB CCD camera (2,560 × 2,048 pixels). The displacement of the former experiments are measured using a Linear Variable Differential Transformer (LVDT) with a measuring range of 25 mm. For the rest of the tests the relative displacement is computed with a 50 mm gauge length digital extensometer generated on the surface of the specimens. The load cell and the LVDT output signals (0 – 10 V) are acquired with a NI-USB-6001 data acquisition card.

Intermediate strain rate (≈10 s^{-1}) and temperature tests are carried out in the same MTS machine as that employed for the room temperature and quasi-static experiments. In this case, graphite paint is used to generate a black dot pattern on the front surface of the specimens, while their back surface is fully covered in the same paint to measure the temperature using an Optris PI400 Infrared (IR) camera. The emissivity of the graphite paint is calibrated using a UT specimen which is painted and heated up to 500°C. The calibration is performed by measuring the temperature with the IR camera on the specimen's painted surface, while using the measurements of a thermocouple mechanically attached to the specimen as a reference value, resulting in an emissivity of 0.73 [46]. A Resistance Heating Device (RHD) equipped with a chiller and

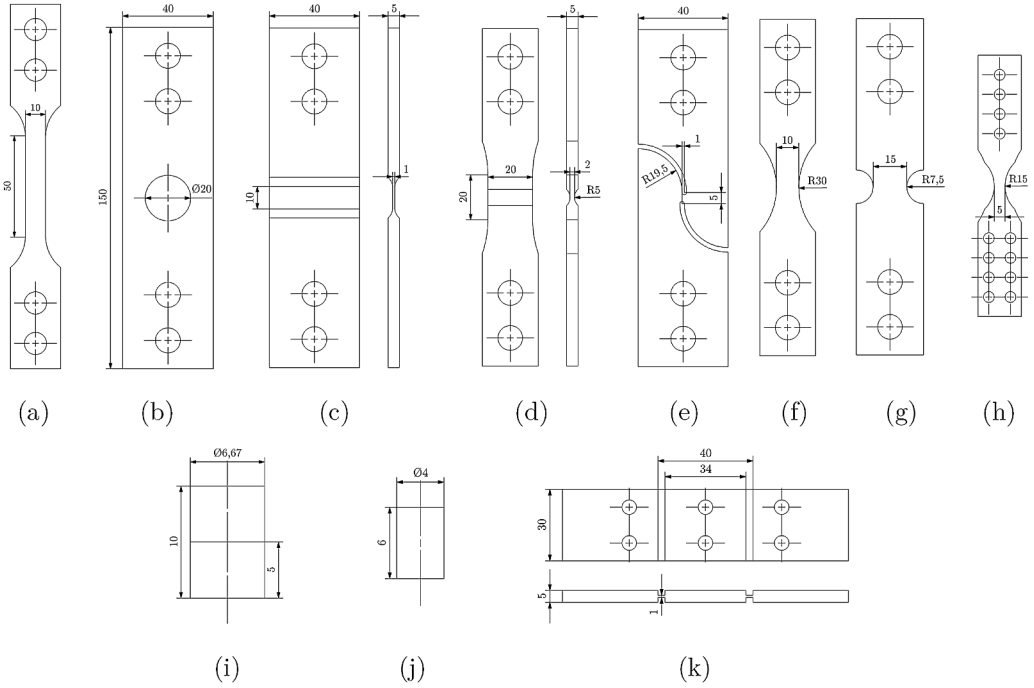

Fig. 2. Specimen geometries used for the material characterization: (a) UT, (b) CH, (c) PS1, (d) PS2, (e) SH2, (f) NT1, (g) NT2, (h) NT3, (i) SC, (j) UC and (k) SH1.

Table 2
Test velocities and frame and data acquisition rates for the different geometries.

Quasi-static		UT	SC	UC	CH	SH1	SH2	PS1	PS2	NT1	NT2	NT3
Test velocity	**[mm/s]**	0.05	0.01	0.01	0.05	0.05	0.05	0.05	0.05	0.05	0.05	–
Image acquisition	**[fps]**	2	–	–	15	2	15	15	15	15	15	–
Data acquisition.	**[Hz]**	2	2	2	15	2	15	15	15	15	15	–
Temperature		UT	SC	UC	CH	SH1	SH2	PS1	PS2	NT1	NT2	NT3
Test velocity	**[mm/s]**	–	–	–	–	–	0.05	0.05	–	0.05	–	–
Image acquisition (HS camera)	**[fps]**	–	–	–	–	–	15	15	–	15	–	–
Image acquisition (IR camera)	**[fps]**	–	–	–	–	–	80	80	–	80	–	–
Data acquisition.	**[Hz]**	–	–	–	–	–	15	15	–	15	–	–
Strain rate		UT	SC	UC	CH	SH1	SH2	PS1	PS2	NT1	NT2	NT3
Test velocity	**[m/s]**	–	–	–	–	–	200	200	–	5, 200	–	3
Image acquisition	**[fps]**	–	–	–	–	–	10k	10k	–	1k, 10k	–	300k
Data acquisition.	**[Hz]**	–	–	–	–	–	1k	1k	–	1k	–	300k

instrumented with a Eurotherm EPC 3016 controller are used for the temperature tests. The desired temperatures, i.e. 100°C, 300°C and 500°C, are maintained constant during the tests with a PID control loop using a signal from the IR camera transmitted to the controller (see Fig. 3). The intermediate strain rate experiments are filmed with a Photron Fastcam-APX RS250K high-speed camera (384 × 496 pixels) and the acquired images are used for the subsequent DIC analysis generating 50 mm virtual extensometer. An external in-house trigger unit was employed to activate both, IR and high speed cameras. All the data, including images and signals acquired during the tests, were synchronized using as a reference the time corresponding to the onset of fracture captured by the high speed camera.

The high strain rate tests (>100 s^{-1}) are carried out using a Split Hopkinson Tensile Bar (SHTB) (see Fig. 4) that is comprised of a 1200 mm striker and 3850 mm input and output bars that are made out of 19.3 mm diameter steel rods. The displacement is measured by means of a 25 mm gauge length digital extensometer generated using DIC on images captured with a Phantom VEO 710 L high-speed camera (256 × 56 pixels). The axial force $F[t]$ is calculated from the transmitted strain histories $\varepsilon[t]$ measured with the strain gage station located on the output bar as:

$$F[t] = AE\varepsilon[t], \tag{1}$$

where $E = 218$ GPa and A are the elastic modulus and the cross-section area of the output bar respectively. A single specimen geometry, NT3 notched tensile specimen (see Fig. 2 (h)), is tested in the SHTB. This specimen is specially manufactured for these tests, with a reduced thickness, from 5 mm to 2 mm, to accommodate the lower load capacity of the experimental setup. The testing velocities and frame and data acquisition rates used for this particular case are provided in Table 2.

3. Anisotropic behavior

The mechanical properties and microstructure of a material undergo changes when subjected to hot rolling processes. Each rolling pass elongates the grains along the RD and work hardens the material, creating different mechanical properties at different directions [4]. In this study, the anisotropic behavior of the 2205 Duplex stainless steel sheet is characterized under quasi-static room temperature conditions. The results obtained in these tests are used to calibrate and assess Hill48 anisotropic yield criterion.

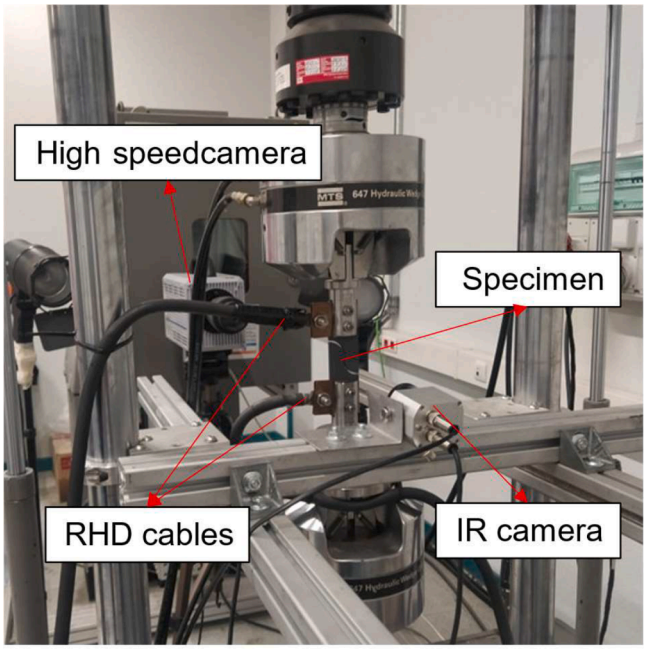

Fig. 3. Setup for the characterization tests performed in quasi-static and intermediate strain rates and at various temperatures (20°C, 100°C, 300°C and 500°C).

3.1. Experiments

A coordinate frame given by the set of unit vectors $\{\boldsymbol{l}, \boldsymbol{t}, \boldsymbol{n}\}$ defining the longitudinal, transversal and thickness directions is assumed in the tensile specimens. The material orthotropy frame is defined by the basis $\{\boldsymbol{i}, \boldsymbol{j}, \boldsymbol{k}\}$, in which the unit vectors coincide with the rolling (RD), transverse (TD) and normal directions (ND) of the sheet respectively.

According to the previous definitions, the UT specimens (see Fig. 2 (a)) that are machined at seven orientations, every 15° with respect to the RD, being θ the angle between $\boldsymbol{i}$ and $\boldsymbol{l}$, have the following stress tensor associated with them:

$$\boldsymbol{\sigma}_\theta = \sigma_\theta\{\cos^2[\theta]\boldsymbol{i}\otimes\boldsymbol{i} + \sin^2[\theta]\boldsymbol{j}\otimes\boldsymbol{j} + 2\sin[\theta]\cos[\theta](\boldsymbol{i}\otimes\boldsymbol{j})^s\}, \tag{2}$$

where σ_θ is the yield stress. The r-values or Lankford coefficients r_θ are defined as:

$$r_\theta = \frac{d\varepsilon^p_{t,\theta}}{d\varepsilon^p_{33}} = -\frac{d\varepsilon^p_{t,\theta}}{\left(d\varepsilon^p_{l,\theta} + d\varepsilon^p_{t,\theta}\right)}, \tag{3}$$

where $d\varepsilon^p$ are the logarithmic plastic strain increments and that are measured with DIC analysis on the surface of the specimens assuming the conservation of volume. The average of the r_θ values obtained in the longitudinal plastic strain range of 5% to 20% are considered.

SC specimens are comprised of two stacked disks forming a cylinder of 5 mm height. (see Fig. 2 (i)). Different strain levels are achieved on the specimens limiting the clamp displacement to 1, 2, 3, 4, 5 and 6 mm. Graphite paste is applied as a lubricant to prevent barreling during the tests, but barreling may still occur. Therefore, the initial and final diameters of the specimens, in rolling and transverse directions, are measured in the center area and from edge to edge to calculate the biaxial r-value r_b:

$$r_b = \frac{d\varepsilon^p_{22}}{d\varepsilon^p_{11}}. \tag{4}$$

Assuming negligible elastic strains, the true strain values in each direction are calculated with $\varepsilon = ln[d_0/d]$, where d_0 is the initial diameter and d is the final diameter.

The cylindrical UC specimens (see Fig. 2 (j)) are machined such that their symmetry axes are aligned with the RD and TD. These tests resulted in the determination of two additional yield stresses, σ^c_0 and σ^c_{90} with identical tensor expression as that in Eq. (2). The true-stress strain curves are obtained neglecting the barreling effect and making use of the volume conservation with:

$$\varepsilon = \ln\left[\frac{h}{h_0}\right] \text{ and } \sigma^c = \frac{Fh}{S_0 h_0}, \tag{5}$$

where h and h_0 are the current and initial heights of the specimen and S_0 is its initial cross-section area.

Small thickness and large width flat-grooved plane strain, or PS1, specimens (see Fig. 2 (c)) are manufactured in the RD and TD, allowing the determination of the σ^{PS}_0 and σ^{PS}_{90} yield stresses, which are identified with the major stresses acting in the loading direction.

The SH1 or Miyauchi shear specimen [47] is a rectangular sheet with two thickness reduced areas that are under shear conditions and three clamping areas as illustrated in Fig. 2 (k). This design allowed balancing the lateral forces and minimizing torsional effects during testing, enabling the measurement of axial force to determine shear stress. SH1 specimens are manufactured in two directions, 0° and 45°, thus obtaining the σ^{SH}_0 and σ^{SH}_{45} yield stresses, from $\sigma^{SH} = F/(2t_0 l_0)$, where l_0

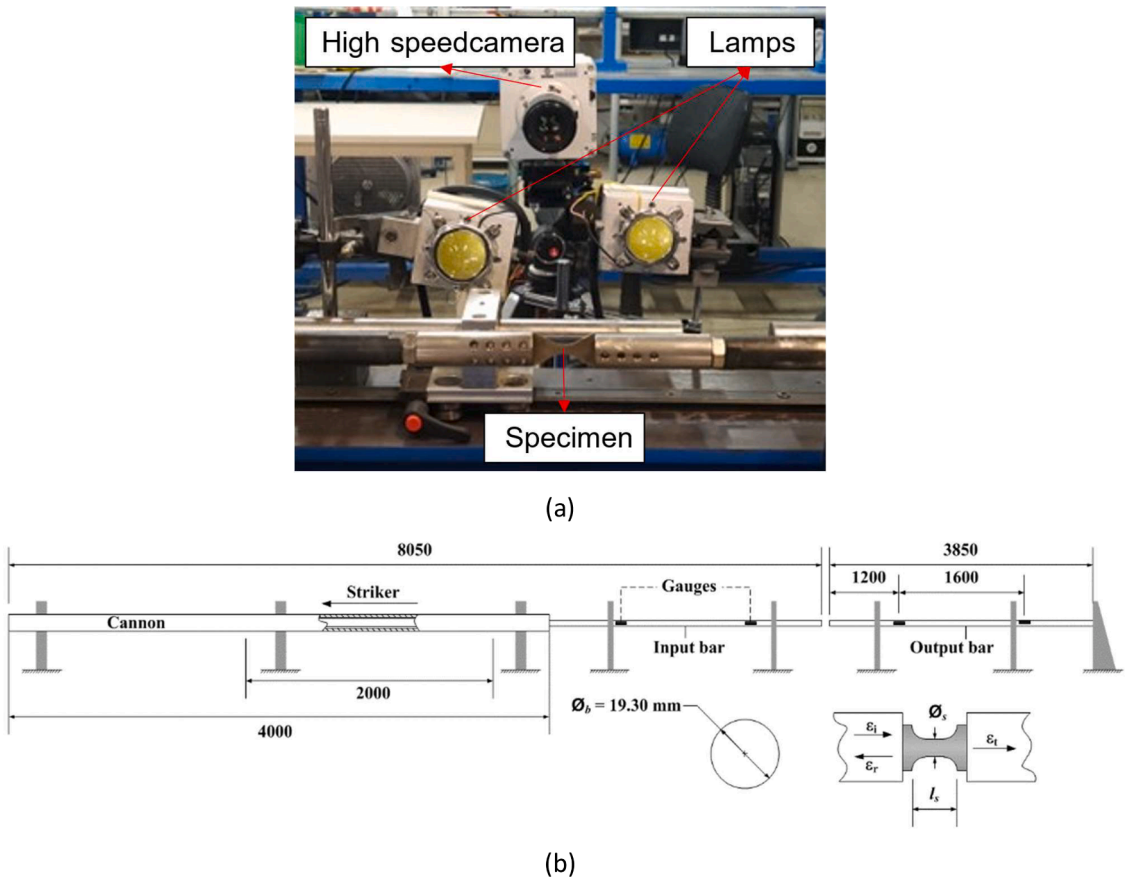

Fig. 4. (a) Setup for the characterization tests performed at high strain rates with the SHTB and (b) schematic representation of the SHTB.

and t_0 are the initial length and thickness of the shear zones respectively. The DIC measurements depicted in Fig. 5 demonstrate homogeneous major and minor strain fields at least up to an applied displacement of 1 mm, which corresponds to a major and minor strain magnitude of around 0.175.

All the experimental results are summarized in Table 3.

3.2. *Hill48 yield function*

Any yield function f can be formally expressed as:

$$f[\boldsymbol{\sigma}] = \overline{\sigma}[\boldsymbol{\sigma}] - \sigma_0, \tag{6}$$

where σ_0 is the reference stress and $\overline{\sigma}$ is the equivalent stress. Being an homogeneous function of degree one, i.e. $\overline{\sigma}[k\boldsymbol{\sigma}] = k\overline{\sigma}[\boldsymbol{\sigma}]$, that satisfies the Euler's theorem for such type of functions, $\overline{\sigma}[\boldsymbol{\sigma}] = \partial\overline{\sigma}[\boldsymbol{\sigma}]/\partial\boldsymbol{\sigma} : \boldsymbol{\sigma}$. To represent the anisotropic yield behavior of the 2205 Duplex stainless

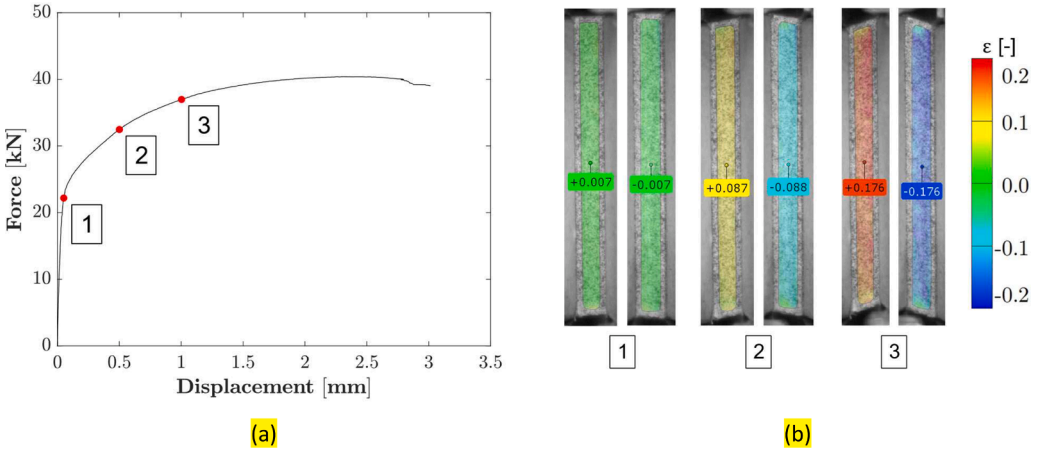

Fig. 5. (a) Marked force-displacement curve for the SH1 specimen and (b) the corresponding major and minor strain fields obtain through DIC.

Table 3
Yield ratios normalized with the reference yield stress σ_0 and Lankford coefficients obtained in the experiments.

		0°	15°	30°	45°	60°	75°	90°	Biaxial
UT	Y_θ [-]	1.000	0.975	0.972	0.980	1.016	1.078	1.123	–
	r_θ [-]	0.292	0.352	0.500	0.715	0.766	0.755	0.725	–
SC	r_b [-]	–	–	–	–	–	–	–	0.455
UC	Y^c_θ [-]	−1.003	–	–	–	–	–	−1.135	–
PS1	Y^{PS} [-]	1.073	–	–	–	–	–	1.204	–
SH1	Y^{SH} [-]	0.527	–	–	0.666	–	–	–	–

steel, Hill48 function has been chosen, which defines the equivalent stress as:

$$\overline{\sigma}[\boldsymbol{\sigma}] = \sqrt{H(\sigma_{11}-\sigma_{22})^2 + F(\sigma_{22}-\sigma_{33})^2 + G(\sigma_{11}-\sigma_{33})^2 + 2N\sigma_{12}^2 + 2L\sigma_{23}^2 + 2M\sigma_{13}^2}, \tag{7}$$

where F, G, H and $N = L = M$, assuming out-of-plane isotropy, are the plasticity parameters. The characterization is designed to explore the behavior of the material under different stress states, providing insights into the material's properties and its response to various conditions. The anisotropic plasticity parameters are calibrated minimizing the error function [10]:

$$\begin{aligned}\mathfrak{E}_y[d,\boldsymbol{\sigma}_\theta,r_i] &= \sqrt{\sum_{i=1}^{n}\left\{d\left[\frac{\sigma_i^{\exp}}{\sigma_0},\frac{\sigma_{\theta_i}}{\sigma_0}\right]\right\}^2} \\ &+\sqrt{\sum_{i=1}^{n_{UT}}\left(1-\frac{\overline{\sigma}[\boldsymbol{\sigma}_{\theta_i}]}{\sigma_0}\right)^2} + \sqrt{\sum_{i=1}^{n}\left(1-\frac{r_{\theta_i}}{r_{\theta_i}^{\exp}}\right)^2},\end{aligned} \tag{8}$$

where the superindex *exp* indicates the experimental data, d is the distance between points, n and n_{UT} are the number of total and UT experiments respectively and θ_i is the direction of the latter with respect to the RD. The minimization problem resulted in the following constants: $F = 0.439$, $G = 0.801$, $H = 0.296$ and $N = 1.495$.

Fig. 6 compares the experimental data from UT, UC, PS1 and SH1 specimens with the predictions made by the calibrated Hill48 and Von Mises yield criteria. The latter did not accurately predict the yield stresses corresponding to the different specimens tested, except for σ_0 and σ_0^c. It underestimated σ_{90}, σ_{90}^C, σ_{90}^{PS} and σ_{45}^{SH} by 10.92%, 11.92%, 7.30% and 13.34% respectively, while overestimating σ_0^{PS} by 6.96%. In contrast, Hill48 criterion provided a better approximation to the experimental yield stresses for the different stress states and directions analyzed. Although this yield criterion sacrifices some accuracy in predicting σ_0 and σ_0^c, it offers better predictions for the rest of the specimens. Overall, Hill48 provided a more than reasonable prediction of the studied yield stresses, with the largest observed error (5.72%) occurring in the RD PS1 specimen.

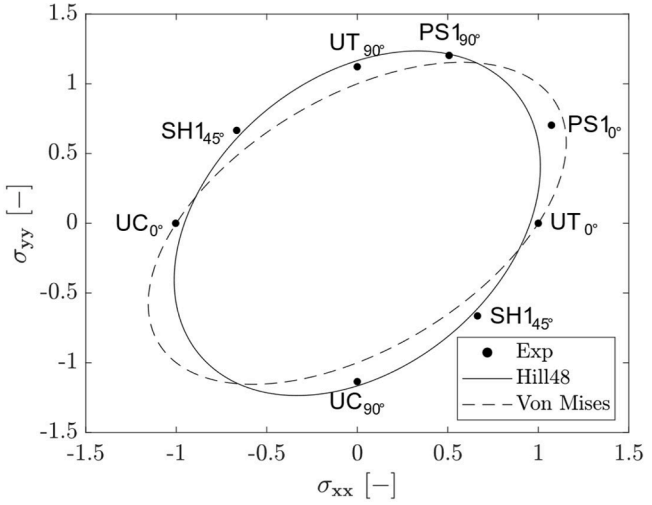

Fig. 6. Hill48 and Von Mises yield surfaces compared to the experimental data.

In Fig. 7 a comparison is presented between the experimentally obtained normalized UT yield stresses and Lankford coefficients at different orientations with respect to the RD and the values predicted by Hill48 anisotropic yield criterion. By minimizing the error in Eq. (8), a compromise between the prediction of the normalized yield stresses and the Lankford ratios is achieved. This resulted in an underestimation of the reference yield stress σ_0, but an improvement in the prediction accuracy as the orientation of the UT specimens approached 45° and an overestimation of the yield stresses as the orientation approached 90°. As for the Lankford coefficients, the opposite trend is observed, i.e. overestimated ratios in the RD, good agreement at 45° and underestimated coefficients at 90°. Nevertheless, Hill48 anisotropic yield model is considered to be accurate enough to capture the anisotropic behavior of the 2205 Duplex stainless steel sheet.

4. Constitutive equations

The additive decomposition of the rate-of-deformation tensor $\boldsymbol{d}$ is assumed as:

$$\boldsymbol{d} = \boldsymbol{d}^e + \boldsymbol{d}^p + \boldsymbol{d}^t, \tag{9}$$

where $\boldsymbol{d}^e$, $\boldsymbol{d}^p$ and $\boldsymbol{d}^t$ are its elastic, plastic and thermal parts. The incremental elastic stress-strain relationship is given by Hooke's law:

$$\begin{aligned}\boldsymbol{\sigma}^\nabla &= \mathbb{C} : \boldsymbol{d}^e \\ &\text{with} \\ \mathbb{C} &= \frac{E}{1+\nu}\left(\mathbb{I} - \frac{1}{3}\boldsymbol{I}\otimes\boldsymbol{I}\right) + \frac{E}{3(1-2\nu)}\boldsymbol{I}\otimes\boldsymbol{I},\end{aligned} \tag{10}$$

where $\boldsymbol{\sigma}^\nabla$ is the Jaumann rate of the Cauchy stress, $\boldsymbol{I}$ and $\mathbb{I}$ are the second and the symmetric fourth-order unit tensors and E and ν are the elastic modulus and Poisson's ratio respectively.

The yield function f is expressed as follows:

$$f\left[\boldsymbol{\sigma},\ \bar{\varepsilon}_p, \dot{\bar{\varepsilon}}_p, T\ \right] = \overline{\sigma}[\boldsymbol{\sigma}] - \sigma_Y\left[\bar{\varepsilon}_p, \dot{\bar{\varepsilon}}_p, T\right], \tag{11}$$

where $\boldsymbol{\sigma}$ is the stress tensor, $\bar{\varepsilon}_p$ is the equivalent plastic strain, $\dot{\bar{\varepsilon}}_p$ is the equivalent plastic strain rate, T is the temperature and σ_Y is the work hardening given by:

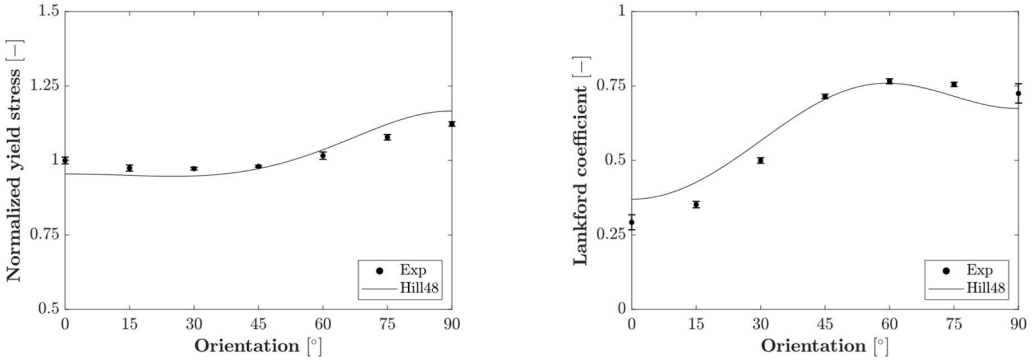

Fig. 7. (a) Comparison of normalized yield stresses and (b) Lankford coefficients under UT at various orientations relative to the RD.

$$\sigma_Y\left[\bar{\varepsilon}_p, \dot{\bar{\varepsilon}}_p, T\right] = \left\{(1-\alpha)K(\varepsilon_0+\bar{\varepsilon}_p)^n + \alpha\left(\sigma_{sat} - (\sigma_{sat}-\sigma_i)e^{-a\bar{\varepsilon}_p^p}\right)\right\}\left\{1 + C\ln\left[\frac{\dot{\bar{\varepsilon}}_p}{\dot{\varepsilon}_0}\right]\right\}\left\{1 - \left(\frac{T-T_r}{T_m-T_r}\right)^m\right\}, \tag{12}$$

where α is the weighing parameter, K, ε_0, n and σ_{sat}, σ_i, a, p are Swift and Hockett-Sherby strain hardening constants respectively, C is the strain rate multiplier, $\dot{\varepsilon}_0$ is the reference strain rate, m is the softening exponent, T_r is the reference temperature and T_m is the temperature at which the material loses its load carrying capacity and is treated as a material constant in this work.

An associative flow rule is considered:

$$\boldsymbol{d}^p = \dot{\lambda}\frac{\partial f}{\partial \boldsymbol{\sigma}}, \tag{13}$$

where $\dot{\lambda}$ is the plastic multiplier. The thermal part of the strain rate is given by:

$$\boldsymbol{d}^t = \alpha\dot{T}\boldsymbol{I}, \tag{14}$$

being α the thermal expansion coefficient. Through work conjugacy, $\boldsymbol{\sigma} : \boldsymbol{d}^p = \overline{\sigma}\dot{\bar{\varepsilon}}_p$, the relationship between the equivalent plastic strain and the plastic multiplier can be defined as $\dot{\bar{\varepsilon}}_p = \dot{\lambda}$. Once the plastic flow is established, the loading/unloading conditions in Kuhn-Tucker form are given for completeness:

$$\dot{\lambda} \geq 0 \; f \geq 0 \; \dot{\lambda} f = 0. \tag{15}$$

The temperature is computed from the heat equation in the thermal solver:

$$\rho C_p \dot{T} = \chi\boldsymbol{\sigma} : \boldsymbol{d}^p + k\nabla^2 T, \tag{16}$$

where χ is the Taylor-Quinney coefficient, ρ is the mass density, C_p is the specific heat and k is the thermal conductivity.

5. Finite element simulations

Numerical simulations have been performed for all specimens used

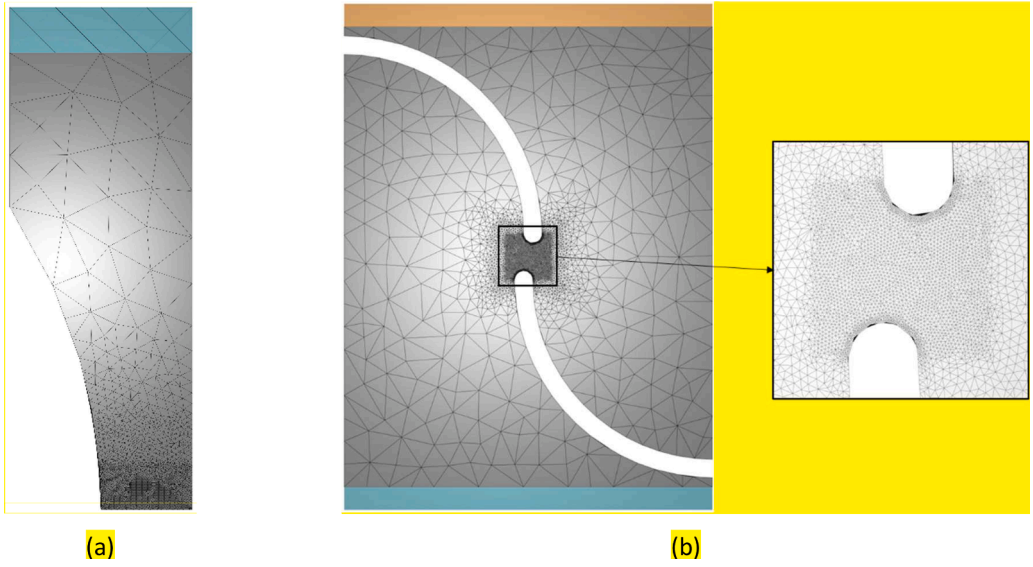

Fig. 8. Examples of the meshes employed in the FE simulations of the characterization tests: (a) NT1 and (b) SH2.

in the work hardening and fracture characterization of the 2205 Duplex stainless steel, including NT1, NT2, NT3, PS1, PS2, CH and SH2 specimens (see Fig. 2). These simulations serve two purposes: firstly, to calibrate the work hardening and validate it together with the anisotropic yield criterion; and secondly, to serve as a platform to extract the loading paths necessary to evaluate different ductile fracture models, which are introduced in the next section.

5.1. Numerical setup

To perform the numerical simulations of the 2205 Duplex stainless steel specimens tested FORGE NxT 4.0 FE software is used. To reduce computational costs, the specimens are simulated using one-eighth of their geometry, except for the SH2 specimen where half of the specimen is used. The geometries are discretized with linear tetrahedral elements in which the velocity fields are enriched with an additional bubble node located in their centroid. The elements have an edge size of 0.1 mm (see Fig. 8), leading to a maximum of ten elements along half of the thickness in the region of interest.

The experimental displacement history of each corresponding test is applied on the upper end nodes. The profiles extracted from the IR images are used to feed the temperature fields in the FE models as initial conditions. The maximum time increment is set to collect at least 1,000 data points. Table 4 presents the elastic constants and the thermophysical properties used for the simulations.

5.2. Work hardening constant identification

To calibrate the eight Swift-Hockett-Sherby strain hardening model parameters (α, K, ε_0, n, σ_{sat}, σ_i, a and p) the difference in NT1 specimen experimental and FE simulation force-displacement curves is minimized with the following cost function:

$$\mathfrak{C}_h = \sqrt{\sum \left(F^{exp} - F^{sim}\right)^2}, \tag{17}$$

Where $\mathfrak{C}_h$ is the minimized error, F^{exp} is the experimental force and F^{sim} is the predicted force. Following the same procedure, the experimental data obtained from the quasi-static NT1 experiments conducted at 100°C, 300°C and 500°C and the room temperature NT1 at 10 s^{-1} and NT3 at >100 s^{-1} are employed to calibrate the thermal softening (T_r, T_m and m) and the strain rate hardening ($\dot{\varepsilon}_0$ and C) parameters. It should be noted that the specimens tested at intermediate and high loading rates undergo adiabatic heating effects. Therefore, the thermal softening is considered in the calibration procedure. The identified material constants are reported in Table 5.

5.3. Model verification

To ensure the reliability of the calibrated computational material model, FE simulations are conducted on various specimen geometries including NT1, NT2, CH, PS1, PS2 and SH2 at room temperature and quasi-static conditions. The force-displacement and local true strain-displacement curves are compared with their corresponding experimental data. The local measurements are obtained from the DIC analysis of two extensometers aligned with the RD and TD (black dots in Fig. 9). In the case of the SH2 specimen, three 1 mm gauge length local extensometers monitored the rotation during the test. The experimental force-displacement curves are obtained following the procedure explained in Section 2.

Fig. 10 compares the force-displacement curves and the local extensometer measurements obtained experimentally and numerically for the NT1, NT2, CH, PS1, PS2 and SH2 specimens. The force-displacement curves showed good agreement in all the specimen geometries considered with the exception of the SH2 specimen, that exhibited poorer agreement overpredicting the force. It is worth noting that all simulations are carried out using the dimensions measured on the specimens through a digital caliper before testing, except in the case of the SH2 specimen, where the nominal geometry is used due to its complex geometry. The local extensometers in both RD and TD also exhibit very good agreement between the numerical and experimental results, indicating the reliability of the material model.

Fig. 11 displays experimental RD and TD strains, as well as, equivalent strain ($\dot{\varepsilon}_{eq} = \sqrt{2/3\boldsymbol{d}^p : \boldsymbol{d}^p}$) contours from the surface DIC analysis corresponding to the onset of fracture for the (a) NT1, (b) and (c) PS2 and (d) SH2 specimens. These measurements provided valuable information about the location of strain localization and fracture initiation. For the NT1 and PS2 specimens (see Fig. 11 (a,b)), the strain is localized in the center of the neck. Fig. 11 (c) indicated that the TD strains are negligible compared to those of the RD, confirming that the fracture initiation area is indeed under plane strain conditions. Finally, the DIC measurements on the SH2 specimen, shown in Fig. 11 (d), suggested that the strain is localized in the gauge area, providing peak values near the edge.

Fig. 12 shows the comparison between the experimental and numerical force-displacement curves of the NT1 (a), PS2 (b) and SH2 (c) quasi-static temperature tests. In general, the tests conducted at 300°C and 500°C exhibited a change in the work hardening which could not be perfectly captured by the model. Despite the limitations of the temperature sensitivity term, the predicted softening effect is consistent with the behavior observed in the experiments. As in the room temperature and quasi-static case, the model overpredicted the last third of the force-displacement curve of the SH2 specimen.

Additionally, Fig. 12 (d,e,f) depict the results of the surface DIC corresponding to the onset of fracture conducted on NT1, PS2 and SH2 specimens respectively at quasi-static conditions and at 500°C, while Fig. 12 (g,h,i) depict the corresponding measured temperature profiles from the IR camera. These figures provided a visual representation of the strain localization and progressive temperature increase in such localized areas during the tests. As in the room temperature tests, in the NT1 and PS2 specimens the strain localization occurred at the center, whereas in SH2 specimen, the strain is localized in the two areas close to the specimen's edge simultaneously. Even if localization phenomena occurred, the IR imaging combined with the RHD ensured constant temperature during the tests making the material model identification process way more consistent and less cumbersome. As these tests are quasi-static, no adiabatic heating effects are observed through IR imaging.

The experimental force-displacement curves of the NT1 and NT3 specimens tested at 10 s^{-1} and >100 s^{-1} are shown in Fig. 13 (a) and Fig. 14 (a) respectively, together with the FE simulation results. Although neither of the responses are able to accurately capture the softening observed for larger displacements, reasonable agreement is observed for both specimens. On the other hand, the mechanical response of the PS2 and SH2 specimens are depicted in Fig. 13 (b,c) in the form of force-displacement curves. The numerical results for both specimens are in good agreement with their corresponding experimental data. Although once again, the softening behavior at the end of the curves is not accurately captured.

Table 4
Elastic constants, thermophysical properties and the Taylor-Quinney coefficient used for the FE simulations.

Temperature [°C]	20	100	200	300	400	500
E [GPa]	185.6	–	–	–	–	–
ν [-]	0.3	–	–	–	–	–
ρ [g/cm^3]	7.732	7.715	7.683	7.652	7.620	7.590
C_p [J/g·K]	0.463	0.403	0.357	0.355	0.373	0.503
k [W/m·K]	13.595	11.692	9.982	11.327	11.827	15.826
α [10^{-5}/K]	–	1.315	1.360	1.410	1.450	–
χ [-]	0.95	–	–	–	–	–

Table 5
Identified material parameters for Swift-Hockett-Sherby work hardening model and for the temperature and strain rate sensitivity terms.

	Material constants							
Strain hardening	α	K	ε_0	n	σ_{sat}	σ_i	a	p
	0.361	1840.5	0.041	0.308	669.5	195.0	100.2	0.702
Thermal softening		T_r			T_m		m	
		20			7202.2		0.500	
Strain rate hardening			$\dot{\varepsilon}_0$				C	
			0.009				0.031	

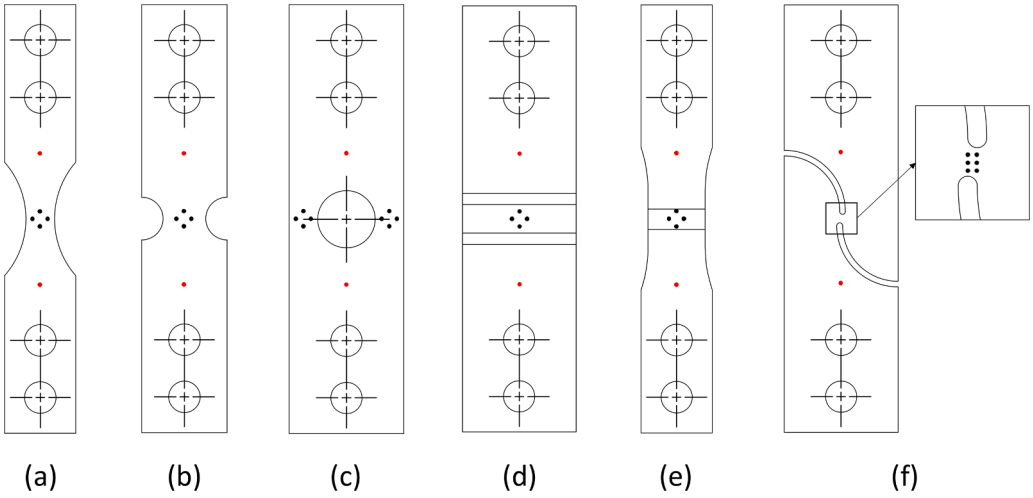

Fig. 9. Location of the macroscopic extensometers for displacement measurement (red dots) and of the local extensometers for local strain measurement (black dots) on (a) NT1, (b) NT2, (c) CH, (d) PS1, (e) PS2 and (f) SH2 specimens.

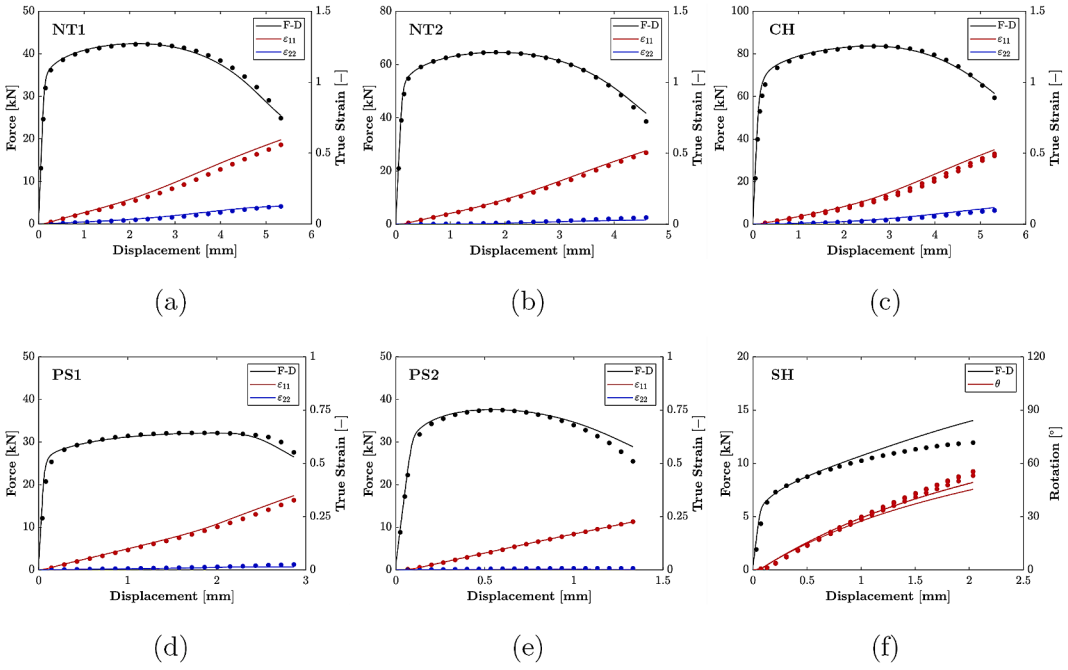

Fig. 10. Comparison of force-displacement curves and local extensometer measurements obtained experimentally (dots) and numerically (lines) for (a) NT1, (b) NT2, (c) CH, (d) PS1, (e) PS2 and (f) SH2 specimens.

Fig. 13 (d,e,f) and Fig. 14 (a) depict the equivalent strain contours measured on the NT1, PS2, SH2 and NT3 specimens using DIC. Consistent with the findings obtained for the quasi-static tests at 500°C, NT1 and PS2 specimens showed strain localization in the center, while SH2 specimen exhibited it near the edge of the specimen. Similarly to what has been observed for the NT1 specimen, the DIC measurements on NT3 specimens tested at high strain rates and room temperature indicate that fracture initiates in the center rather than in the edges. IR images in Fig. 13 (g,h,i) provide an insight of the adiabatic heating effect on the strain localization areas of the specimens, which according to the surface

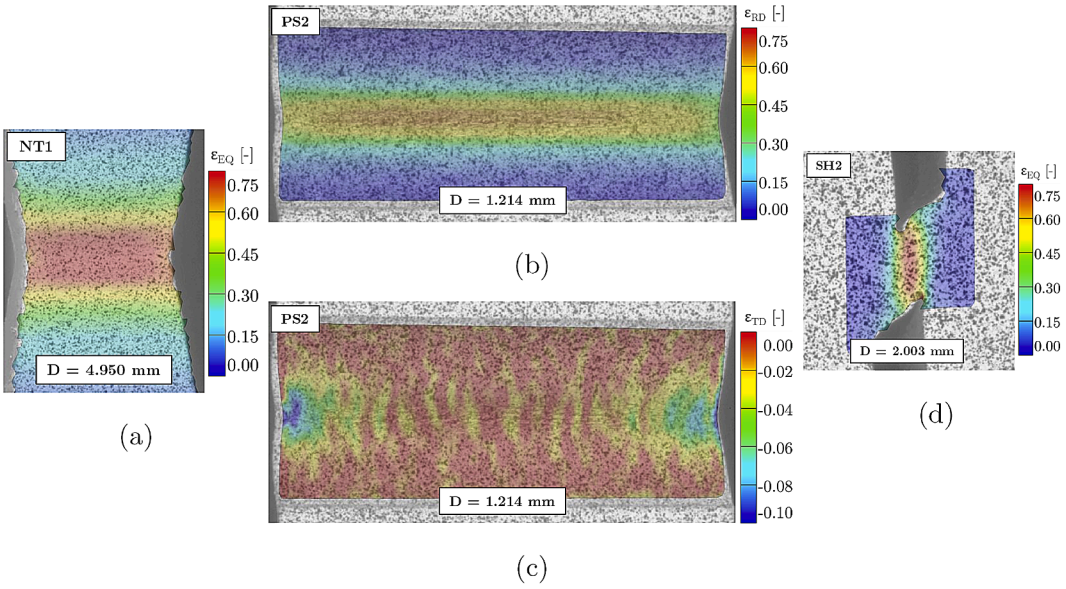

Fig. 11. DIC analysis corresponding to the onset of fracture displacement D, boxed in the figures, for the (a) NT1 specimen showing equivalent strain contours, the PS2 specimen showing (b) RD and (c) TD strain distributions and (d) the SH2 specimen showing equivalent strain contours, all at quasi-static and room temperature conditions.

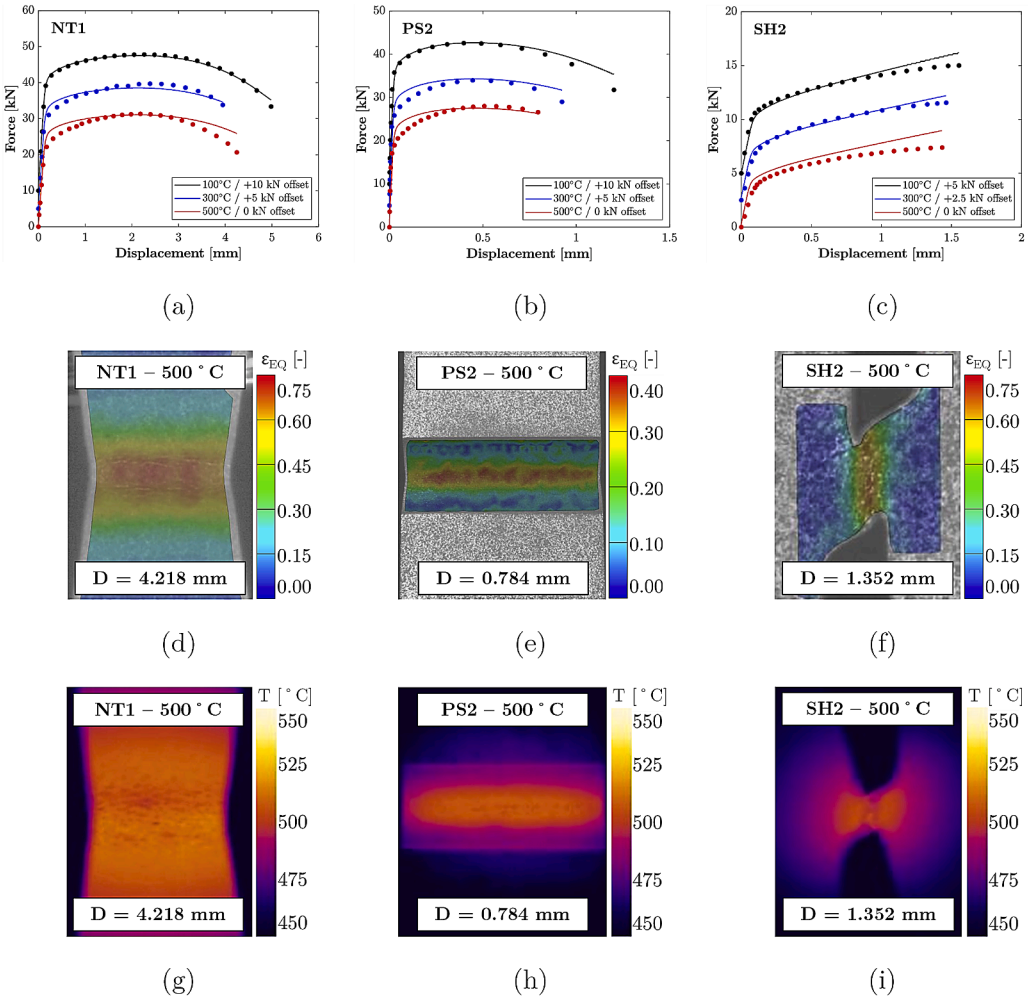

Fig. 12. Comparison of force-displacement curves obtained experimentally (dots) and numerically (lines) under quasi-static conditions at 100°C, 300°C and 500°C for the (a) NT1, (b) PS2 and (c) SH2 specimens. Equivalent strain and temperature contours from surface DIC and IR imaging respectively obtained at 500°C for the (d,g) NT1, (e,h) PS2 and (f,i) SH2 specimens.

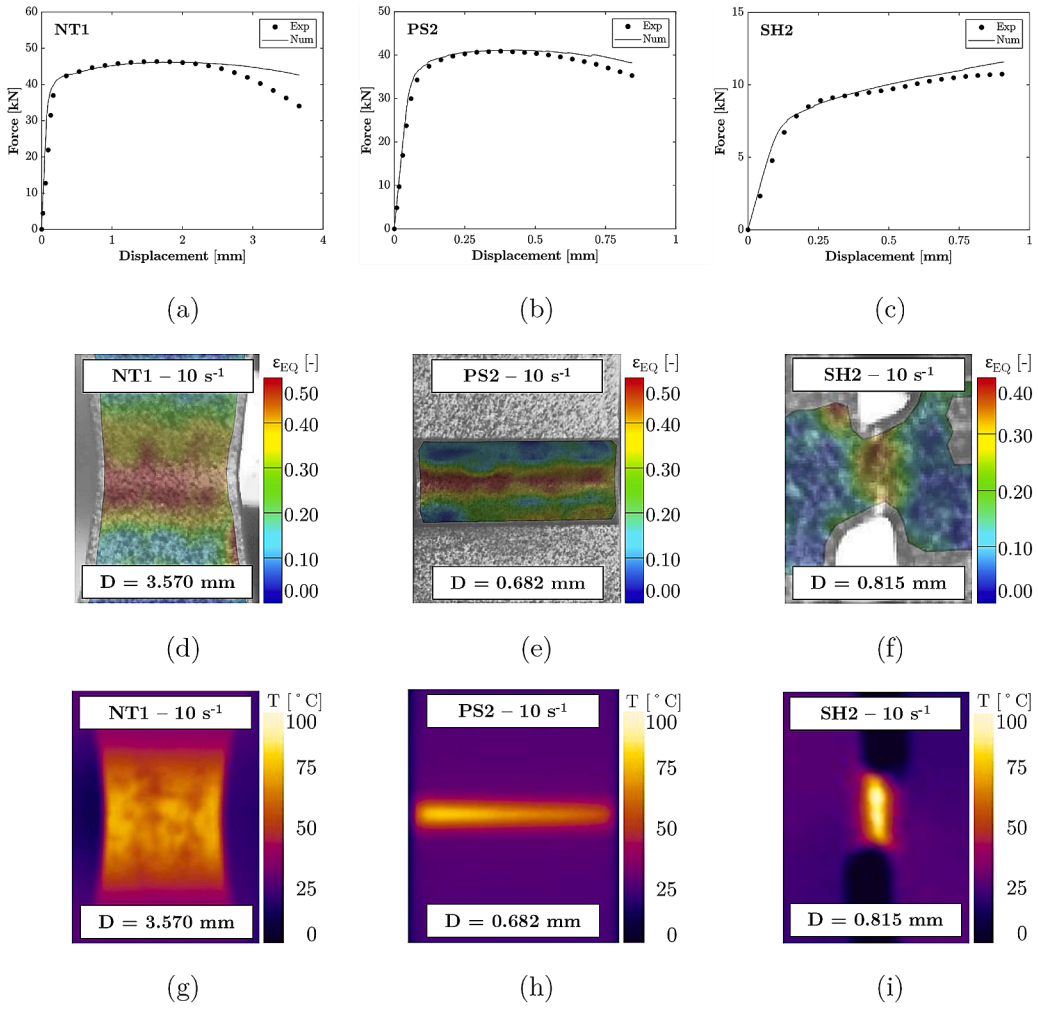

Fig. 13. Comparison of force-displacement curves obtained experimentally and numerically at room temperature and 10 s^{-1} with (a) NT1, (b) PS2 and (c) SH2 specimens. DIC and IR measurements of the last images acquired prior to fracture from the (g) NT1, (h) PS2 and (i) SH2 specimens tested at 10 s^{-1}.

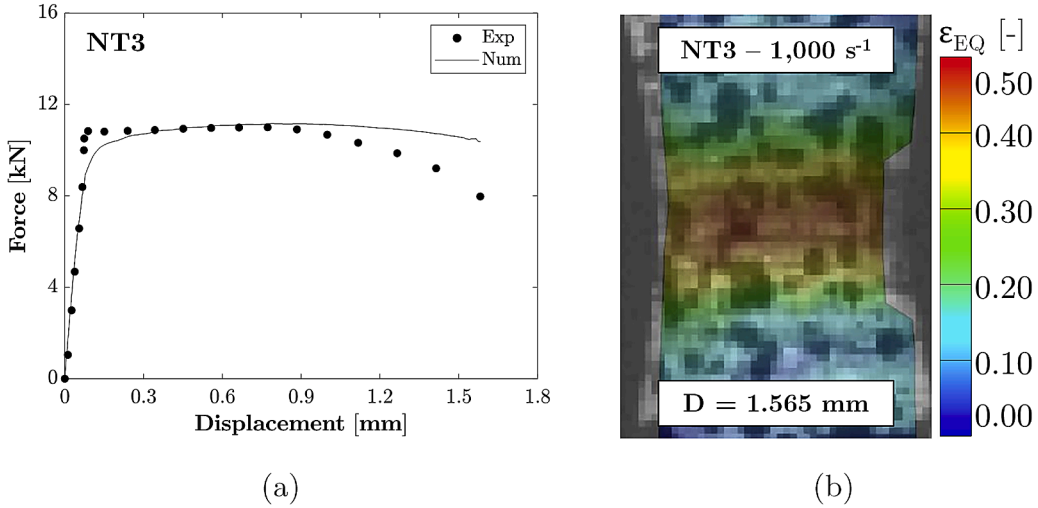

Fig. 14. (a) Comparison of force-displacement curves obtained experimentally and numerically and (b) DIC measurements obtained from the NT3 specimen tested at >100 s^{-1} and at room temperature.

measurements reaches temperatures of at least 100°C instants prior to the onset of fracture.

6. Fracture modelling

6.1. Ductile fracture initiation models

The stress state of an isotropic material can be characterized with the stress triaxiality η and the Lode angle parameter $\bar{\theta}$ defined as:

$$\eta = \frac{\boldsymbol{\sigma} : \boldsymbol{I}}{3\bar{\sigma}_{VM}} \text{ and } \bar{\theta} = 1 - \frac{2}{\pi}\text{acos}\left[\frac{27}{2}\frac{det[\boldsymbol{\sigma}]}{\bar{\sigma}_{VM}^3}\right], \tag{18}$$

where $\bar{\sigma}_{VM} = \sqrt{3/2\text{dev}[\boldsymbol{\sigma}] : \text{dev}[\boldsymbol{\sigma}]}$ is the equivalent Von Mises stress.

To include the effects for non-proportional loading paths, a damage indicator D^{exp} is defined:

$$D^{exp} = \int_0^{\bar{\varepsilon}_p^f} \frac{1}{\bar{\varepsilon}_f^{pr}\left[\eta, \bar{\theta}, \dot{\bar{\varepsilon}}_p, T\right]} d\bar{\varepsilon}_p, \tag{19}$$

where $\bar{\varepsilon}_p^f$ is the equivalent plastic strain corresponding to the onset of fracture and $\bar{\varepsilon}_f^{pr}$ is the fracture strain for proportional loadings, a functional of the stress state, strain rate and temperature histories. The material's damage indicator D^{exp}, has a value of zero in its initial undeformed state and reaches unity at the onset of fracture.

In this study two ductile fracture initiation models are considered, DF2016 [32] and Hosford-Coulomb [33], that are expressed with two alternative expressions of the proportional fracture strain. DF2016 criterion reads:

$$\bar{\varepsilon}_{f,DF}^{pr}[\eta, \bar{\theta}] = \frac{C_3}{(f_I - f_{III})^{C_1}\left(\left\langle \frac{\eta + C_4 f_I + C_5}{\frac{1}{3} + C_4\frac{2}{3} + C_5} \right\rangle\right)^{C_2}}, \tag{20}$$

while Hosford-Coulomb criterion is defined as:

$$\bar{\varepsilon}_{f,HC}^{pr}[\eta, \bar{\theta}] = b\left(\frac{1+c}{\left\{\frac{1}{2}(|f_I - f_{II}|^a + |f_{II} - f_{III}|^a + |f_I - f_{III}|^a)\right\}^{1/a} + c(2\eta + f_I + f_{III})}\right)^{1/n} \tag{21}$$

where $\langle\blacksquare\rangle = \max[0, \blacksquare]$ are the Macaulay brackets, C_1, C_2, C_3 and a, b, c, n are their respective constants and f_I, f_{II} and f_{III} are Lode angle parameter dependent trigonometric functions:

$$\begin{aligned} f_I[\bar{\theta}] &= \frac{2}{3}\cos\left[\frac{\pi}{6}(1 - \bar{\theta})\right], \\ f_{II}[\bar{\theta}] &= \frac{2}{3}\cos\left[\frac{\pi}{6}(3 + \bar{\theta})\right], \\ f_{III}[\bar{\theta}] &= -\frac{2}{3}\cos\left[\frac{\pi}{6}(1 + \bar{\theta})\right]. \end{aligned} \tag{22}$$

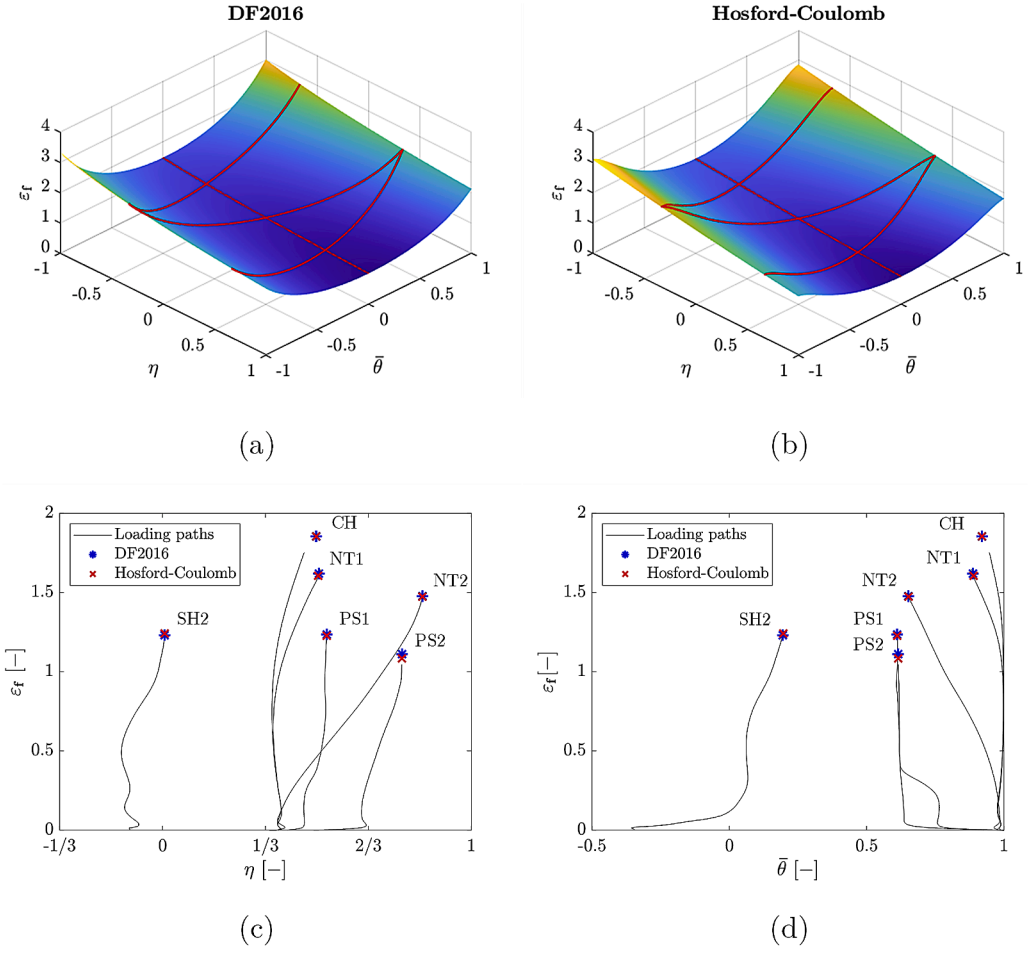

Fig. 15. Predicted fracture surfaces for proportional loading using (a) DF2016 and (b) Hosford-Coulomb ductile fracture initiation criteria and the loading paths of the NT1, NT2, CH, PS1, PS2 and SH2 specimens (c,d).

Table 6
Identified material constants for DF2016 and Hosford-Coulomb ductile fracture initiation criteria under quasi-static conditions.

DF2016					
Temperature [°C]	C_1	C_2	C_3	C_4	C_5
20	5.189	0.396	2.319	0.906	1.775
Hosford-Coulomb					
Temperature [°C]	a	b	c	n	
20	1.643	2.102	0.004	0.032	
100	1.621	2.053	0.000	0.029	
300	1.909	0.793	0.002	0.023	
500	1.632	1.433	0.001	0.026	

6.2. Loading paths to fracture

The fracture initiation criteria are calibrated using the extensively used hybrid experimental-numerical approach [21]. The so-called loading paths (η, $\bar{\theta}$ and $\bar{\varepsilon}_p$ histories) shown in Fig. 15 (c,d) are extracted from the location with the largest equivalent plastic strain value at the onset of the fracture displacement in each of the six different specimens (NT1, NT2, CH, PS1, PS2 and SH2) and the following error function is minimized:

$$\mathfrak{E}_f = \sqrt{\sum_i^N (1 - D^{exp})^2}, \tag{23}$$

where $\mathfrak{E}_f$ is the minimized error, N is the number of specimens used and D^{exp} is the damage indicator computed from the hybrid numerical-experimental approach. The fracture criteria constants are reported in Table 6 and the fracture surfaces corresponding to proportional loading conditions are depicted in Fig. 15 (a) for DF2016 and in Fig. 15 (b) for Hosford-Coulomb.

Hosford-Coulomb criterion yielded slightly more accurate predictions than DF2016, at least for the specimens examined (see Fig. 15 (c,d)). In both cases, the CH specimen exhibited the largest error, overestimating the fracture strain by only 5.94% relative to the experimental value.

The difference between the proportional fracture loci is observed at the extreme Lode angle parameter values of the -1 and 1. While DF2016 criterion predicted an exponential increase of the strain at these locations (see Fig. 15 (a)), Hosford-Coulomb criterion predicted a flatter fracture surface (see Fig. 15(b)). However, to provide a more quantitative comparison between the results obtained with each model, the relative errors of every specimen and the overall average are calculated as follows:

$$E_{avg} = \frac{1}{N}\sum_i^N E_N = \frac{1}{N}\sum_i^N \left| 1 - \frac{\bar{\varepsilon}_p^{f,sim}}{\bar{\varepsilon}_p^{f,exp}} \right|, \tag{24}$$

where the superindices *sim* and *exp* indicate the predicted and experimental equivalent plastic fracture strains and $N = \{\text{CH, NT1, NT2, PS1, PS2, SH2}\}$ is the number of specimens used.

The relative error analysis shown in Fig. 16 indicated that overall, Hosford-Coulomb ductile fracture criterion performed better, with average relative errors of 3.2% and 2.9% for DF2016 and Hosford-Coulomb, respectively. However, it seemed that DF2016 gave lower error values for lower stress triaxialities (CH, NT1, NT2 and PS2). Despite the good performance of both models, for the sake of simplicity, only Hosford-Coulomb ductile fracture model has been chosen for its modification, allowing to account for the temperature and strain rate effects on the material's fracture behavior.

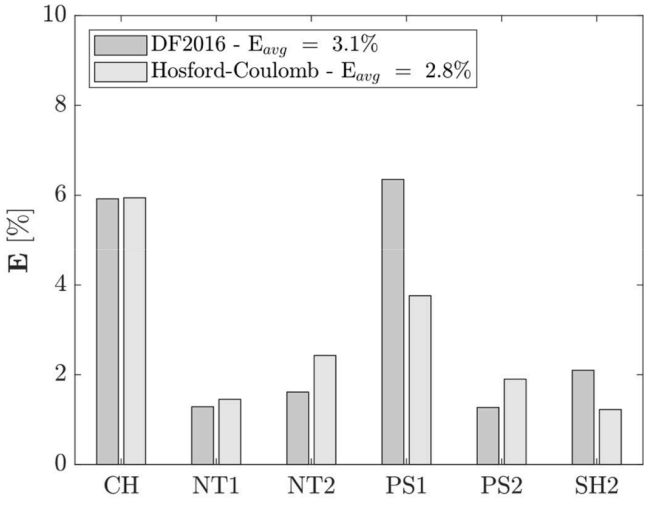

Fig. 16. Errors calculated for DF2016 and Hosford-Coulomb ductile fracture initiation criteria using the data of the CH, NT1, NT2, PS1, PS2 and SH2 specimens.

6.3. Temperature sensitivity

A simple and straightforward adjustment has been introduced in the fracture criterion to account for the temperature effects. It consists in a stepwise linear interpolation of the material constants for the temperature range studied while for the temperatures out of range the material constants obtained at the nearest studied temperature are used. Hosford-Coulomb model is calibrated separately for each of the temperatures, 100°C, 300°C and 500°C, with the loading paths collected from NT1, PS2 and SH2 specimens under quasi-static conditions, following the same process as that described in the previous section. The material constants of such calibration are reported in Table 6.

The new loading paths obtained at the tested temperatures for each specimen are compared with their counterparts obtained in room temperature conditions in Fig. 17. On the other hand, the fracture strain, which shows a decreasing trend with the increasing temperature for the three specimens, is shown in Fig. 18 (a). However, this trend is mildly altered in the case of the NT1 specimen, which presented a lower fracture strain at 300°C than at 500°C. This could be attributed to the phase transformation that typically occurs in Duplex stainless steels around 300°C, from $\alpha + \gamma$ to $\alpha + \gamma + \alpha'$ [48], which may have caused the loss of ductility of the material due to the prolonged exposure to the objective temperature, 300°C in this case. However, this effect is not observed for the PS2 and SH2 specimens, making it challenging to confirm. Further microstructural analysis would be required to draw any definitive conclusions.

Fig. 18 (b) depicts the predicted plane stress fracture envelopes at different temperatures using Hosford-Coulomb model. These envelopes illustrate the expected trend of decreasing fracture strain with increasing temperature, except for the envelope at 300°C, which deviates from the trend at $\eta = 1/3$ (uniaxial tension) due to the NT1 specimen's fracture strain. As a result, the whole envelope is flattened, which is translated in a less stress state dependent fracture locus.

6.4. Loading rate sensitivity

The tests conducted to calibrate the temperature sensitivity have been conducted under controlled constant-temperature conditions employing the RHD and PID loop control system. However, in the case of the tests utilized for the loading rate sensitivity calibration (NT1, NT3, PS2 and SH2), where a consistent crosshead velocity is applied, the presence of necking followed by severe strain localization within the specimens led to non-uniform strain rates throughout these tests (see Fig. 13 and Fig.14). Consequently, the methodology outlined in the preceding section could not be directly applied, as the identified

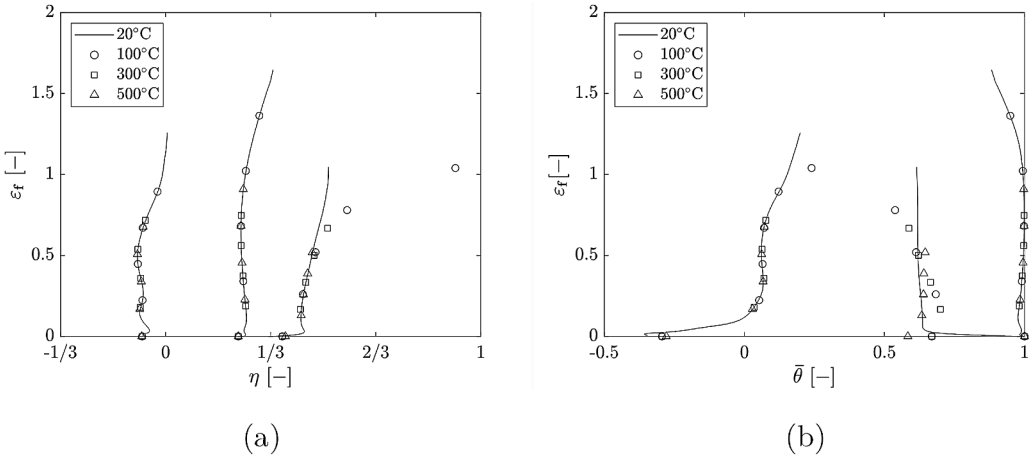

Fig. 17. Loading paths of the NT1, PS2 and SH2 specimens at the tested temperatures as a function of the (a) stress triaxiality and the (b) Lode angle parameter.

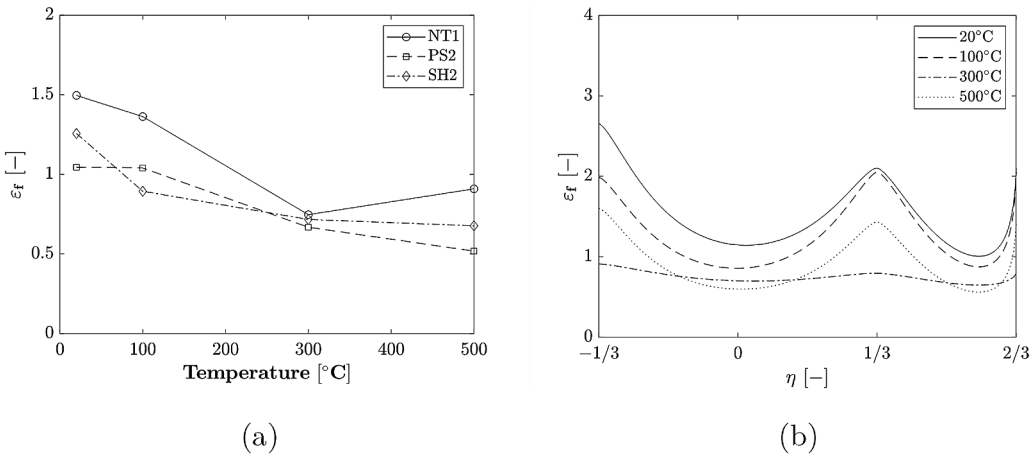

Fig. 18. (a) Evolution of the fracture strain with temperature for NT1, PS2 and SH2 specimens and (b) plane stress fracture envelopes predicted by Hosford-Coulomb model at 20°C, 100°C, 300°C and 500°C.

material constants would not correspond to a specific strain rate value. To tackle this challenge, we have modified Hosford-Coulomb constants independently as:

$$a'\left[\dot{\bar{\varepsilon}}_p\right] = a[T]\; k_1\left[\dot{\bar{\varepsilon}}_p\right], \tag{25}$$

$$b'\left[\dot{\bar{\varepsilon}}_p\right] = b[T]\; k_1\left[\dot{\bar{\varepsilon}}_p\right]\; k_2\left[\dot{\bar{\varepsilon}}_p\right], \tag{26}$$

$$c'\left[\dot{\bar{\varepsilon}}_p\right] = c[T]\; k_1\left[\dot{\bar{\varepsilon}}_p\right], \tag{27}$$

$$n'\left[\dot{\bar{\varepsilon}}_p\right] = n[T]\; k_1\left[\dot{\bar{\varepsilon}}_p\right], \tag{28}$$

introducing the following specifically designed strain rate dependent functions to adjust the material constants:

Table 7
Identified material constants for Hosford-Coulomb ductile fracture model in room temperature conditions and at various strain rates (intermediate and high).

	Rate-dependent Hosford-Coulomb			
Parameters	a'	b'	c'	n'
C_1	28.865	2.754	36.329	23.996
C_2	0.200	0.926	1.616	0.375
C_3	–	4.415	–	–
C_4	–	1.843	–	–
C_5	–	1.020	–	–

$$k_1\left[\dot{\bar{\varepsilon}}_p\right] = 1 + C_2 \tanh\left[\frac{\dot{\bar{\varepsilon}}_p}{C_1}\right], \tag{29}$$

$$k_2\left[\dot{\bar{\varepsilon}}_p\right] = 1 + C_3\, \exp\left[-\frac{\left(\log\left[\dot{\bar{\varepsilon}}_p\right] - C_4\right)^2}{2{C_5}^2}\right], \tag{30}$$

where a', b', c' and n' are the updated material constants and C_i with $i = [1, 5]$ are material parameters specific to each one of the updated constants. It should be noted that to account for the combined loading rate effects, this is temperature and strain rate, Hosford-Coulomb model constants are temperature dependent and, as stated earlier, are implemented as a stepwise linear function that interpolates linearly between the values corresponding to the known temperatures.

The material constants that now consider the strain rate's influence on Hosford-Coulomb model are determined through calibration, using the loading paths from NT1, NT3, PS2 and SH2 specimens subjected to intermediate and high strain rates employing the same methodology as in the previous subsections (see Table 7). The proposed functions in Eqs. (25 – 30) combined with the optimized material constants, establish a model in which the parameter evolution stabilizes to approximately 1,000 s^{-1} as the strain rate increases. Conversely, for lower strain rates ($<$0.01 s^{-1}), these functions guide the material constants towards values obtained under quasi-static conditions.

The calibration tests, which aim to explore the influence of loading

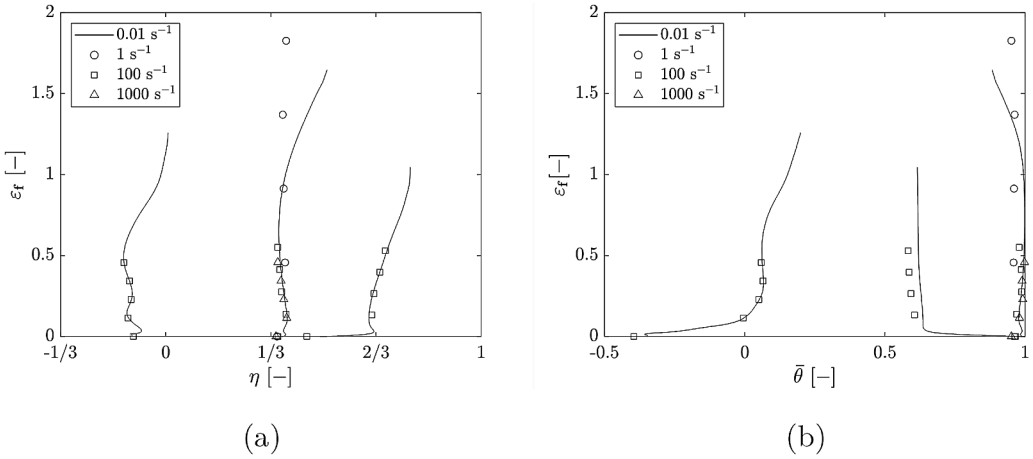

Fig. 19. Loading paths of the NT1, NT3, PS2 and SH2 specimens at the tested loading rates as a function of the (a) stress triaxiality and the (b) Lode angle parameter.

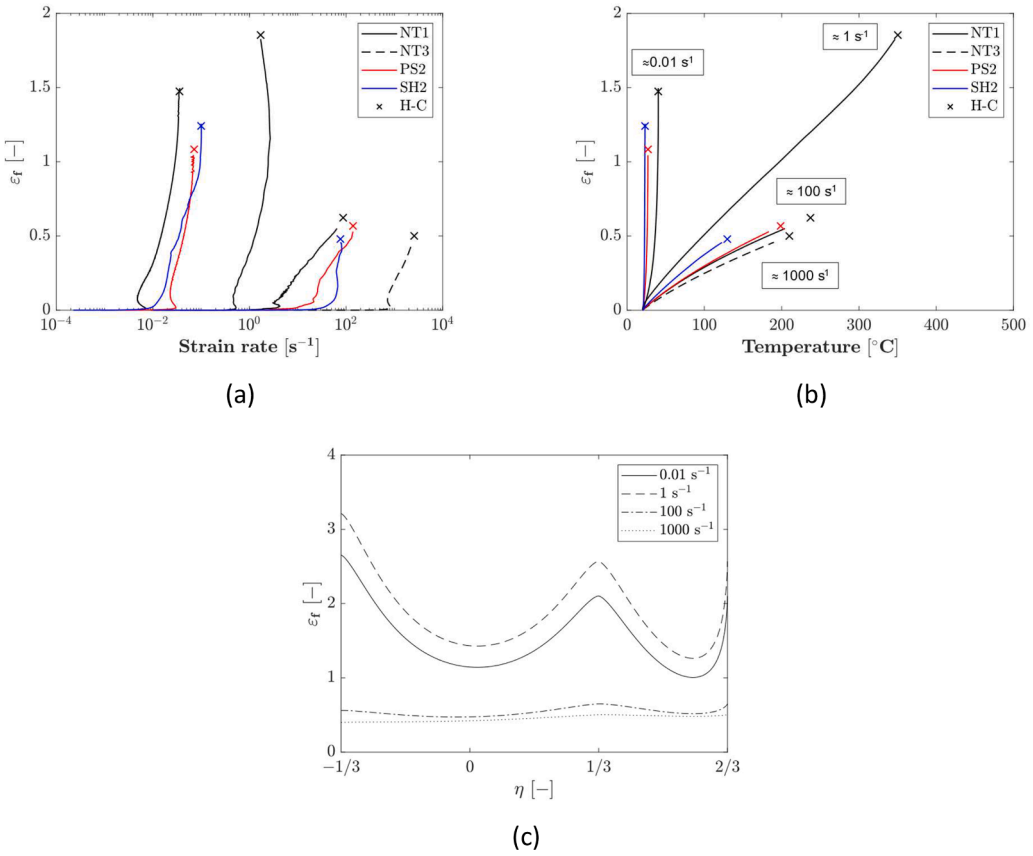

Fig. 20. (a) Strain rate paths and (b) temperature paths up to fracture strain of NT1, PS2, SH2 and NT3 specimens and (c) plane stress fracture envelopes predicted by rate- and temperature- Hosford-Coulomb model at 0.01 s^{-1} (solid line), 1 s^{-1} (dashed line), 100 s^{-1} (dashed-dotted line) and 1,000 s^{-1} (dotted line).

rate on the fracture behavior of the 2205 Duplex stainless steel, are conducted at three different rates: quasi-static (≈0.01 s^{-1}), intermediate (≈100 s^{-1}) and high (≈1,000 s^{-1}). These tests consistently exhibited a reduction in fracture strain as the strain rate increased (see Fig. 20 (a)). Interestingly, the intermediate loading rate tests intended to reach roughly to a strain rate of 10 s^{-1}. Nevertheless, higher strain rates than that anticipated are attained. As a result, the conducted tests spanned through roughly 0.01 s^{-1}, 100 s^{-1} and 1,000 s^{-1}, leaving a significant gap between 0.01 s^{-1} and 100 s^{-1}. To address this, additional tests are carried out on NT1 specimens subjected to a nominal strain rate of 1 s^{-1} in the UTM. The results obtained are included in the loading rate sensitivity calibration and are depicted in Fig. 20, while the obtained loading paths are shown in Fig. 19 and compared with the ones obtained in quasi-static conditions.

A noteworthy phenomenon to highlight is the adiabatic heating effect observed during the simulation of the NT1 specimens used for the loading rate sensitivity calibration (see Fig. 20 (b)). In the quasi-static tests, the low velocity allows sufficient time for the heat generated in the specimen to dissipate through convection with the surrounding air. Conversely, in the two fastest tests conducted at 100 s^{-1} and 1,000 s^{-1}, the heat generation is limited due to the significantly reduced ductility. Interestingly, the additional test introduced to bridge the gap between

0.01 s^{-1} and 100 s^{-1}, is the specimen that has developed the largest plastic strains and consequently, also achieved the largest temperature values (see Fig. 20 (b)).

The proportional plane stress fracture loci at different constant strain rates, shown in Fig. 20 (c), illustrate an initial increase in fracture strain followed by a significant reduction. The loading rate sensitivity calibration tests have unveiled a more pronounced and uneven impact on fracture behavior compared to the temperature sensitivity. As shown Fig. 20 (b), the shape of the fracture surface remains relatively consistent across different temperatures, except for the anomaly observed at 300°C. However, the influence of strain rate indicates that increasing the strain rate leads to a flattening of the fracture envelope, equalizing the fracture strain across the stress triaxiality η range depicted in Fig. 20 (c).

7. Conclusions

Two main objectives are established for this work, (i) to determine the mechanical behavior at various temperatures and strain rates of a 2205 Duplex stainless steel sheet in terms of anisotropic behavior, work hardening and fracture behavior and (ii) to propose a simple yet effective phenomenological material modelling procedure, accurate enough to reproduce the experimentally observed mechanical behavior through FE simulations. To do so, the following aspects have been analyzed:

- Anisotropic thermo-viscoplasticity: Various stress states and orientations have been tested to determine the anisotropic behavior of the 2205 Duplex stainless steel. Hill48 anisotropic yield model provides a better approximation of the yield loci at different stress states and orientations compared to Von Mises isotropic yield criterion. It accurately predicts the yield loci for most stress states, except for a slight overestimation in one particular specimen and orientation. On the other hand, the thermomechanical behavior of 2205 Duplex stainless steel has been determined through experimental tests conducted under different stress states, temperatures and strain rates. Swift-Hockett-Sherby model has demonstrated the ability to reproduce accurately the work hardening of the studied material. To further enhance the model's precision in capturing the material's behavior, additional terms proposed by Johnson & Cook are incorporated to account for the effects of strain rate and temperature. This augmentation endowed the model with the necessary flexibility to accurately replicate the thermomechanical response of the material.
- Loading rate dependent fracture behavior: The fracture behavior of the material has been extensively investigated under various stress states, temperatures and strain rates. Comparing the performance of Hosford-Coulomb ductile fracture model with DF2016 in terms of the average error committed in the fracture prediction of each specimen, it is found that Hosford-Coulomb yields slightly more accurate predictions of the fracture loci of the material in quasi-static and room temperature conditions overall. Temperature tests revealed a progressive decrease in the strain to fracture as the temperature increased, except for an anomaly observed at 300°C, which could be attributed to a phase transformation effect. Hosford-Coulomb model effectively adapted to the fracture surfaces obtained at different temperatures, with its material constants modified using linear interpolation between known temperature values. Furthermore, the strain rate is found to exert a significant influence on fracture behavior. An initial increase of the fracture strain is observed up to 1 s^{-1} followed by a reduction stage at intermediate strain rates, which reached saturation between 100 s^{-1} and 1,000 s^{-1}. To accurately capture this effect within Hosford-Coulomb model, the material constants are modified using a set of functions that effectively replicated the fracture loci of the tested specimens.
- Exhaustive characterization: This research presents an exhaustive characterization of a 5 mm thick 2205 Duplex stainless steel sheet, with the aim of elucidating and modelling its anisotropic thermo-viscoplastic behavior and loading rate-dependent fracture behavior. A plethora of characterization tests are conducted to achieve this objective, covering a spectrum of orientations relative to the RD of the metal sheet and encompassing various stress states, temperatures and strain rates. Despite the substantial volume of experimental data collected, the selected models chosen to replicate the observed behavior have been successfully calibrated, offering a precise representation of the material's response within the examined conditions.

In summary, this work presents a comprehensive characterization and modelling approach for the mechanical behavior of a 2205 Duplex stainless steel. It provides valuable insights into the material's anisotropic behavior, work hardening and fracture behavior, while accurately reproducing its overall mechanical response within a FE framework. Apart from the findings shared in this investigation, this study also offers an invaluable and extensive experimental material data that is not usually available.

CRediT authorship contribution statement

D. Abedul: Writing – original draft, Methodology, Investigation. **L. Galdos:** Writing – review & editing, Supervision. **E. Sáenz de Argandoña:** Writing – original draft, Supervision. **F. Galvez:** Supervision, Resources. **B. Erice:** Writing – review & editing, Supervision, Methodology, Investigation.

Declaration of competing interest

The authors declare the following financial interests/personal relationships which may be considered as potential competing interests:

Lander Galdos reports financial support was provided by European Commission. Lander Galdos reports financial support was provided by Basque Government. Borja Erice reports financial support was provided by State Agency of Research. If there are other authors, they declare that they have no known competing financial interests or personal relationships that could have appeared to influence the work reported in this paper.

Data availability

Data will be made available on request.

Acknowledgements

The authors gratefully acknowledge the financial support provided by the European Commission Research Fund under the project name: INTELLCUTPROCESS (899331), and by the Basque Government through ELKARTEK research funding under the project name: DIGICUT (KK-2019/00071). The author Borja Erice would like to acknowledge the support from the Grant RYC2021-033241-I funded by MCIN/AEI/10.13039/501100011033 and by "European Union NextGenerationEU/PRTR".

References

[1] Demmel P, Hoffmann H, Golle R, Intra C, Volk W. Interaction of heat generation and material behaviour in sheet metal blanking. CIRP Ann Manuf Technol 2015;64(1):249–52.
[2] Canales C, Boman R, Ponthot JP. Thermomechanical simulations of blanking process operated over a wide range of punch velocities. J Phys Conf Ser 2018;1063(1).
[3] Behrens B-A, Brunotte K, Wester H, Kock C, Kildonaviciute D. Determination of temperature dependence in Modified-Mohr-Coulomb failure model for process simulation of shear cutting. IOP Conf Ser Mater Sci Eng 2022;1238(1):012028.
[4] Mohammadzehi S, Mirzadeh H, Sohrabi MJ, Roostaei M, Mahmudi R. Elucidating the effects of cold rolling route on the mechanical properties of AISI 316L austenitic stainless steel. Mater Sci Eng A 2023;865(January):144616.

[5] Hill R. A theory of the yielding and plastic flow of anisotropic metals. Proc R Soc London Ser A Math Phys Sci 1948;193(1033):281–97.
[6] Yan Y, Wang H, Li Q. The inverse parameter identification of Hill 48 yield criterion and its verification in press bending and roll forming process simulations. J Manuf Process 2015;20:46–53.
[7] Kacem A, Laurent H, Thuillier S. Influence of temperature on the formability of an aluminum alloy. ESAFORM 2021 2021;14:1–10.
[8] Saanouni K, Belamri N, Autesserre P. Finite element simulation of 3D sheet metal guillotining using advanced fully coupled elastoplastic-damage constitutive equations. Finite Elem Anal Des 2010;46(7):535–50.
[9] Barlat F, et al. Plane stress yield function for aluminum alloy sheets - Part 1: theory. Int J Plast 2003;19(9):1297–319.
[10] D. Banabic, *Sheet Metal Forming Processes*. 2010.
[11] Yoshida F, Hamasaki H, Uemori T. A user-friendly 3D yield function to describe anisotropy of steel sheets. Int J Plast 2013;45:119–39.
[12] Li X, Roth CC, Tancogne-Dejean T, Mohr D. Rate- and temperature-dependent plasticity of additively manufactured stainless steel 316L: characterization, modeling and application to crushing of shell-lattices. Int J Impact Eng 2020;145 (January):103671.
[13] Rahmaan T, Noder J, Abedini A, Zhou P, Butcher C, Worswick MJ. Anisotropic plasticity characterization of 6000- and 7000-series aluminum sheet alloys at various strain rates. Int J Impact Eng 2020;135(September 2019):103390.
[14] Tisza M, Lukács Z, Kovács P, Budai D. Some recent developments in sheet metal forming for production of lightweight automotive parts. J Phys Conf Ser 2017;896 (1).
[15] Yoshida F, Hamasaki H, Uemori T. Modeling of anisotropic hardening of sheet metals including description of the Bauschinger effect. Int J Plast 2015;75:170–88.
[16] Williams BW, Simha CHM, Abedrabbo N, Mayer R, Worswick MJ. Effect of anisotropy, kinematic hardening, and strain-rate sensitivity on the predicted axial crush response of hydroformed aluminium alloy tubes. Int J Impact Eng 2010;37 (6):652–61.
[17] Berisha B, Hora P, Wahlen A, Tong L. A combined isotropic-kinematic hardening model for the simulation of warm forming and subsequent loading at room temperature. Int J Plast 2010;26(1):126–40.
[18] Hollomon H. Tensile deformation. Aime Trans 1945;12(4):1–22.
[19] Ludwik P. Elemente der technologischen mechanik. Verlag von Jul. Springer; 1909.
[20] Swift HW. Plastic instability under plane stress. J Mech Phys Solids 1952;1(1): 1–18.
[21] Erice B, Roth CC, Mohr D. Stress-state and strain-rate dependent ductile fracture of dual and complex phase steel. Mech Mater 2018;116:11–32.
[22] Hensel A, Spittel T. Kraft- und Arbeitsbedarf bildsamer formgebungsverfahren. VEB DeutscherVerlag fur Grundstoffindustrie; 1978.
[23] Johnson GR, Cook WH. A computational constitutive model and data for metals subjected to large strain, high strain rates and high pressures. In: Seventh Int. Symp. Ballist.; 1983. p. 541–7.
[24] Li X, et al. Plastic deformation and ductile fracture of L907A ship steel at increasing strain rate and temperature. Int J Impact Eng 2023;(November 2022):104515.
[25] Pandya KS, Roth CC, Mohr D. Strain rate and temperature dependent fracture of aluminum alloy 7075: experiments and neural network modeling. Int J Plast 2020; 135:102788.
[26] Rice JR, Tracey DM. On the ductile enlargement of voids in triaxial stress fields. J Mech Phys Solids 1969;17(3):201–17.
[27] Mackenzie AC, Hancock JW, Brown DK. On the influence of state of stress on ductile failure initiation in high strength steels. Eng Fract Mech 1977;9(1).
[28] Johnson GR, Cook WH. Fracture characteristics of three metals subjected to various strains, strain rates, temperatures and pressures. Eng Fract Mech 1985;21(1): 31–48.
[29] Wierzbicki T, Xue L. On the effect of the third invariant of the stress deviator on ductile fracture. Int J Fract 2005. vol. Impact and.
[30] Xue L. Damage accumulation and fracture initiation in uncracked ductile solids subject to triaxial loading. Int J Solids Struct 2007;44(16):5163–81.
[31] Bai Y, Wierzbicki T. A new model of metal plasticity and fracture with pressure and Lode dependence. Int J Plast 2008;24(6):1071–96.
[32] Lou Y, Chen L, Clausmeyer T, Tekkaya AE, Yoon JW. Modeling of ductile fracture from shear to balanced biaxial tension for sheet metals. Int J Solids Struct 2017; 112:169–84.
[33] Mohr D, Marcadet SJ. Micromechanically-motivated phenomenological Hosford-Coulomb model for predicting ductile fracture initiation at low stress triaxialities. Int J Solids Struct 2015;67–68:40–55.
[34] Roth CC, Mohr D. Effect of strain rate on ductile fracture initiation in advanced high strength steel sheets: experiments and modeling. Int J Plast 2014;56:19–44.
[35] Huh H, Kim SB, Song JH, Lim JH. Dynamic tensile characteristics of TRIP-type and DP-type steel sheets for an auto-body. Int J Mech Sci 2008;50(5):918–31.
[36] Dunand M, Mohr D. Predicting the rate-dependent loading paths to fracture in advanced high strength steels using an extended mechanical threshold model. Int J Impact Eng 2017;108:272–85.
[37] Cerik BC, Choung J. Rate-dependent combined necking and fracture model for predicting ductile fracture with shell elements at high strain rates. Int J Impact Eng 2020;146(July):103697.
[38] Wu P, Lou Y, Chen Q, Ning H. Modeling of temperature- and stress state-dependent yield and fracture behaviors for Mg-Gd-Y alloy. Int J Mech Sci 2022;229(July): 107506.
[39] Clausen AH, Børvik T, Hopperstad OS, Benallal A. Flow and fracture characteristics of aluminium alloy AA5083-H116 as function of strain rate, temperature and triaxiality. Mater Sci Eng A 2004;364(1–2):260–72.
[40] Erice B, Gálvez F, Cendón DA, Sánchez-Gálvez V. Flow and fracture behaviour of FV535 steel at different triaxialities, strain rates and temperatures. Eng Fract Mech 2012;79:1–17.
[41] Khan AS, Liu H. Strain rate and temperature dependent fracture criteria for isotropic and anisotropic metals. Int J Plast 2012;37:1–15.
[42] Oliferuk W, Maj M, Litwinko R, Urbański L. Thermomechanical coupling in the elastic regime and elasto-plastic transition during tension of austenitic steel, titanium and aluminium alloy at strain rates from 10 -4 to 10 -1 s -1. Eur J Mech A/ Solids 2012;35:111–8.
[43] Agirre J, Abedul D, Saenz de Argandoña E, Otegi N, Galdos L, Erice B. An automatic thermo-mechanical testing apparatus for metal forming applications. Int J Impact Eng 2023;182(July 2022).
[44] Dunand M, Mohr D. Hybrid experimental-numerical analysis of basic ductile fracture experiments for sheet metals. Int J Solids Struct 2010;47(9):1130–43.
[45] Roth CC, Mohr D. Determining the strain to fracture for simple shear for a wide range of sheet metals. Int J Mech Sci 2018;149(October):224–40.
[46] Ibarretxe U. Hot stamping of high strength aluminum alloys. Mechanics and Industrial Production, Faculty of Engineering, Mondragon Unibertsitatea; 2023.
[47] Abspoel M, Scholting ME, Lansbergen M, An Y, Vegter H. A new method for predicting advanced yield criteria input parameters from mechanical properties. J Mater Process Technol 2017;248(December 2016):161–77.
[48] Knyazeva M, Pohl M. Duplex steels: part I: genesis, formation, structure. Metallogr Microstruct Anal 2013;2(2):113–21.